

**MICROFLUIDIC DEVICE FOR CONTINUOUS DEFORMABILITY BASED  
SEPARATION OF CIRCULATING TUMOR CELLS**

by  
Chao Jin

B.E., Zhejiang University, Hangzhou, China, 2012

A THESIS SUBMITTED IN PARTIAL FULFILLMENT OF  
THE REQUIREMENTS FOR THE DEGREE OF

MASTER OF APPLIED SCIENCE

in

THE FACULTY OF GRADUATE AND POSTDOCTORAL STUDIES  
(Mechanical Engineering)

THE UNIVERSITY OF BRITISH COLUMBIA

(Vancouver)

September 2014

© Chao Jin, 2014

## Abstract

Circulating tumor cells have been implicated as potential seeds of cancer metastasis and have strong prognostic and diagnostic value in cancer therapy. The primary challenge in CTC characterization is their extreme rarity in circulation relative to leukocytes. Conventional strategies employ CTC immunoenrichment that is highly selective but may fail to enrich for CTCs with poor antigen expression. However, CTCs exhibit unique morphological characteristics that distinguish them from leukocytes and deformability-based sorting mechanisms represent a compelling label-free CTC enrichment strategy. Our group previously reported the microfluidic ratchet mechanism capable of highly selective deformability based cell separation without clogging. Here, we developed a continuous version of this process that obviates the need for microvalves and operate with dramatically increased throughput. Implementation of the microfluidic ratchet consists of a matrix of funnel constrictions with microchannels for flow control. The openings of the funnel constrictions are gradually reduced from the bottom row to the top row. Cells enter at the bottom-left of the funnel matrix and are driven by a rightward flow simultaneously as a vertical oscillatory flow. Each cell traverses through the funnel matrix in a step-wise diagonal path until reaching a limiting funnel size. CTCs are the least deformable cells and reach their limiting funnel size relatively quickly. Leukocytes are more deformable and travel to a smaller funnel region. Finally, erythrocytes are extremely deformable and exit through the top row. We evaluated the selectivity of this mechanism using UM-UC13 bladder cancer cells doped into whole blood from healthy donors. UM-UC13 cells were enriched by  $\sim 10^4$  relative to leukocytes, with  $\sim 90\%$  capture efficiency, and thus demonstrate significantly greater selectivity than separation based solely on size. We used the microfluidic ratchet device to enumerate CTCs from 58 samples with 52 patients with castrate resistant prostate cancer, in parallel with CellSearch, and 6 healthy control samples. The CTC capture rate is significantly higher for our device, which detected  $\geq 5$  CTCs in 67.3% of patients with an average count of 256, while the CellSearch system detected  $\geq 5$  CTCs in 40.4% of patients with an average count of 74.

## **Preface**

A version of Section 1.1 and 1.2 has been published in *C. Jin, S. M. McFaul, S. P. Duffy, X. Deng, P. Tavassoli, P. C. Black, and H. Ma, "Technologies for label-free separation of circulating tumor cells: from historical foundations to recent developments," Lab. Chip, vol. 14, no. 1, p. 32, 2014.*

Section 2.1 describes a ratchet mechanism for providing pressure asymmetry required in deforming a cell through a tapered pore. An initial version of this model was originally developed by Dr. Hongshen Ma, and early modeling was conducted by Quan Guo and Sarah McFaul. Here I adapted this model for continuous deformability based separation of circulating tumor cells.

Chapter 6 and Chapter 7 describe CTC detection in patient samples. Antibodies used for immunofluorescent staining is optimized by Sunyoung Park. Richard Ang assisted in Confocal based spectrum scanning and analysis. Number of CTCs is counted by Sunyoung Park. I conducted patient sample processing, immunofluorescent staining, and scanning under confocal microscope.

# Table of Contents

<b>Abstract</b> .....	<b>ii</b>
<b>Preface</b> .....	<b>iii</b>
<b>Table of Contents</b> .....	<b>iv</b>
<b>List of Tables</b> .....	<b>vi</b>
<b>List of Figures</b> .....	<b>vii</b>
<b>List of Abbreviations</b> .....	<b>x</b>
<b>Acknowledgements</b> .....	<b>xi</b>
<b>Dedication</b> .....	<b>xii</b>
<b>Chapter 1: Introduction</b> .....	<b>1</b>
1.1 Performance Metrics.....	2
1.2 Literature Review .....	4
1.2.1 Biophysical and Biomechanical Properties of CTCs .....	4
1.2.2 Hydrodynamic Chromatography .....	6
1.2.3 Dielectrophoresis.....	8
1.2.4 Filtration .....	9
1.2.5 Post-separation Analysis.....	11
1.3 Microfluidic Ratchet Mechanism for Deformability based Cell Separation .....	14
1.4 Goals of the Thesis.....	14
<b>Chapter 2: Microfluidic Ratchet Mechanism for Cell Separation</b> .....	<b>15</b>
2.1 Clogging in Traditional Filtration System .....	15
2.2 Microfluidic Ratchet Mechanism .....	16
2.2.1 Physical Asymmetry of Ratchet Mechanism.....	16
2.2.2 Cell Separation using Ratchet Mechanism.....	20
2.3 Continuous Cell Separation using Microfluidic Ratchets.....	20
<b>Chapter 3: Device Design and Modeling</b> .....	<b>22</b>
3.1 Device Design.....	22
3.2 System Hydrodynamic Resistance Analysis .....	24
3.3 Resistance of Funnel Matrix .....	29
3.4 Resistance of Supporting Microchannels and Flow Rate .....	31
3.4.1 Resistance of Supporting Microchannels .....	31
3.4.2 Flow Rate Calculation .....	33

3.5 Reliable Cell Sorting.....	34
3.5.1 Variation in Oscillation Resistance of Cutoff Funnels .....	34
3.5.2 Variation in Total Oscillation Flow Rate .....	38
3.6 Summary .....	39
<b>Chapter 4: Fabrication and Experimental Procedures.....</b>	<b>41</b>
4.1 Fabrication of Silicon Masters .....	41
4.2 Fabrication of PDMS Devices .....	42
4.3 Sample Preparation .....	43
4.4 Experimental Setup and Procedure .....	43
<b>Chapter 5: System Characterization and Discussion.....</b>	<b>45</b>
5.1 System Characterization .....	45
5.2 Cell Diameter .....	47
5.3 Pressure Optimization.....	47
5.4 Performance Dependence on Doping Ratio.....	50
5.5 Cell Viability.....	52
5.6 Size and Deformability based Separation versus Size-only Separation.....	53
5.7 Discussion.....	55
<b>Chapter 6: CTC Detection in Patient Samples.....</b>	<b>57</b>
6.1 Sample Preparation and Post-separation Analysis for Patient Samples.....	57
6.1.1 Patient Sample Preparation.....	57
6.1.2 Immunofluorescent Staining .....	58
6.1.3 Image Scanning and Analysis using Confocal Microscope.....	58
6.2 Results from CRPC Patients .....	59
6.3 Discussion.....	61
6.3.1 Confocal based Spectrum Analysis .....	61
6.3.2 EpCAM Expression.....	61
<b>Chapter 7: Conclusion .....</b>	<b>63</b>
7.1 Summary of Results.....	63
7.2 Limitations .....	63
7.3 Future Works.....	63
<b>References .....</b>	<b>65</b>

## List of Tables

### Chapter 1

Table 1.1 Post-separation analysis and requirements. ....	13
---	----

### Chapter 3

Table 3.1 Device components and resistance. ....	32
--	----

### Chapter 5

Table 5.1 Relationship of pressure difference of cutoff funnels and the yield of cancer cells. .....	49
---	----

Table 5.2 Relationship of pressure difference of cutoff funnels and the depletion ratio of leukocytes. ....	49
--	----

Table 5.3 Relationship of pressure difference of cutoff funnels and the enrichment. ....	49
--	----

Table 5.4 Relationship of doping ratio and system performance.....	51
--	----

Table 5.5 Yield of cancer cells and enrichment calculated from Tabel 5.4.....	51
---	----

Table 5.6 Numbers of live cells and dead cells at the cancer outlet of the device in 8 random experiments. ....	52
--	----

Table 5.7 Comparison of expected enrichment of size based separation and enrichment of separation using ratchet device when reaching the same yield.....	55
---	----

### Chapter 6

Table 6.1 Data comparison between Microfluidic ratchet device and CellSearch. ....	60
--	----

# List of Figures

## Chapter 1

- Figure 1.1 Conceptual schematic of a cell separation system. ....3
- Figure 1.2 Forces acting on a particle in a straight microchannel. Shear gradient lift force and wall-effect lift force are orthogonal to the direction of primary flow. Drag force is in the direction of primary flow and will be zero when the particle's velocity equals the flow velocity.....8
- Figure 1.3 Dielectrophoresis: (A) Positive DEP; (B) Particle equilibrium point in pDEP; (C) Negative DEP; (D) Particle equilibrium point in nDEP.....9
- Figure 1.4 Filtration mechanisms: (A) Weir, (B) Pillar, (C) Pore..... 10
- Figure 1.5 Microfluidic ratchet: Large stiff cells are prevented from transiting through the pores in forward flow (A) while smaller more deformable cells are prevented from returning under reverse flow (B)..... 14

## Chapter 2

- Figure 2.1 Working principle of a traditional membrane filter (A) and how the resistance changes as process time goes by (B). .... 15
- Figure 2.2 Three dimensional view of a cell deforming through a funnel constriction. the internal pressure of the cell is denoted  $P_{int}$  while  $P_1$  and  $P_2$  are the pressures acting on the leading and trailing membranes of the cell respectively. .... 17
- Figure 2.3 Top view (A) and front view (B) of a cell deforming through a funnel. .... 17
- Figure 2.4 Schematic of forces acting on a curved membrane. (A) Leading edge membrane. (B) Trailing edge membrane. .... 18
- Figure 2.5 Deformation of a single cell through microscale funnel constrictions in forward (A) and backward (B) directions..... 19
- Figure 2.6 Operation of the microfluidic ratchet mechanism. Cells are introduced into the bottom-left of the funnel matrix and travel in a step-wise diagonal path before reaching a limiting funnel size. CTCs (orange), leukocytes (blue), and erythrocytes (red) each follow a distinct path in the matrix. .... 21

## Chapter 3

- Figure 3.1 Schematic draw of microfluidic ratchet device. The device consists of sample inlet, buffer inlet, sampler outlet, waste outlet, oscillation microchannels and central sorting area. .... 23
- Figure 3.2 Device operation schematic: Cells are introduced through the sample inlet to the bottom left. Inside the funnel array cells are alternately pushed forward and backward.

(A) Forward flow part. (B) Backward flow part. ....	24
Figure 3.3 Hydrodynamic resistance analysis of the device for flow control. ....	25
Figure 3.4 Cutoff funnels and pressure difference of cutoff funnels. ....	27
Figure 3.5 Circuit analysis of the oscillation flow (A). The voltage source can equal to a current source when oscillation channels' resistance is dominant (B). ....	28
Figure 3.6 Pressure drop in 6 $\mu\text{m}$ -funnel gap when pressure is applied on the bottom face.	30
Figure 3.7 Flow velocity in 6 $\mu\text{m}$ -funnel gap. ....	30
Figure 3.8 Model of ten 12 $\mu\text{m}$ -funnel gaps in series and flow velocity simulation under 10,000 Pa pressure difference in horizontal direction. ....	31
Figure 3.9 Flow simulation of the buffer channel in COMSOL. (A) Physics-controlled mesh of buffer inlet channel. (B) Simulation of flow velocity inside the channel. ....	32
Figure 3.10 Flow velocity simulation of 6 $\mu\text{m}$ -funnel gaps with a cell at the bottom. ....	35
Figure 3.11 Flow velocity simulation of 6 $\mu\text{m}$ -funnel gaps with a cell in a funnel. ....	35
Figure 3.12 The relationship between the oscillation resistance of cutoff funnels and throughput. ....	37
Figure 3.13 Schematic analysis of the filter resistance when no cell is captured (A) and when all the funnels at the top right are occupied by cells (B). ....	38
Figure 3.14 A continuous cell separation device based on the microfluidic ratchet mechanism. ....	40

## Chapter 4

Figure 4.1 Fabrication process of silicon masters. ....	42
Figure 4.2 Fabrication process of PDMS devices ....	42
Figure 4.3 The pressure board. (1) Forward pressure regulators. (2) Backward pressure regulators. (3) Forward pressure manifolds along with solenoid valves. (4) Backward pressure manifolds along with solenoid valves. (5) Microcontroller and circuit board system. ....	44

## Chapter 5

Figure 5.1 Micrograph of cell distribution in sorting region: Leukocytes are stained with Hoechst (blue) and UC13 are stained with Calcein AM (green). ....	46
Figure 5.2 Fluorescent image of the CTC outlet well (A) and leukocyte outlet well (B). UM-UC13 cells were stained with Calcein AM (green) and leukocytes were stained with Hoechst (Blue). ....	46
Figure 5.3 Size distributions of leukocytes (blue) and UC13 (red). ....	47
Figure 5.4 Relationship of pressure difference of cutoff funnels and the yield of cancer cell (A), and enrichment (B). ....	50
Figure 5.5 Relationship of doping ratio and system performance. (A) Number of cancer cell	

captured and its relationship with number cancer cell doped. (B) Enrichment and its relationship with doping ratio of leukocytes to cancer cells. ....	52
Figure 5.6 Culture of cancer cells captured from device. ....	53
Figure 5.7 Distributions of UC13 and leukocyte, and the method to calculate enrichment of size based separation with a pore size. ....	54
Figure 5.8 Comparison of expected enrichment of size based separation and enrichment of separation using ratchet device when reaching the same yield. ....	55

**Chapter 6**

Figure 6.1 Work flow of CTC separation using patient samples. ....	57
Figure 6.2 Spectrum analysis for CTC identification. CTCs are identified with DAPI+, CK or EpCAM+, CD45-, while leukocytes are identified DAPI+, CK-, EpCAM- and CD45+. ....	59
Figure 6.3 Comparison of captured CTC numbers between Microfluidic ratchet device and CellSearch. P01 to P52 are patient samples; and C01 to C06 are healthy control samples. ....	59
Figure 6.4 Comparison of captured CTC numbers between patients showing no progression and progression in cancer using CellSearch system and Microfluidic ratchet device. .	60
Figure 6.5 Example images of CTC and leukocyte. ....	61

## List of Abbreviations

BSA	Bovine Serum Albumin
CTC	Circulating Tumor Cell
CK	Cytokeratin
DEP	Dielectrophoresis
EMT	Epithelial–Mesenchymal Transition
EpCAM	Epithelial Cellular Adhesion Molecule
FDA	Food and Drug Administration
mCRPC	metastatic Castration Resistant Prostate Cancer
PDMS	Polydimethylsiloxane
PBS	Phosphate Buffered Saline

## **Acknowledgements**

First and foremost, I would like to express my sincere gratitude to my supervisor Dr. Hongshen Ma for his continuous support of my study and research. His patience, enthusiasm, and immense knowledge helped me a lot in all the time of research and writing of this thesis. I am honored to have had this opportunity to work together with him.

Secondly I want to thank Sarah McFaul who taught me microfabrication process, cancer cell culture procedure, microfluidic device design principle and helped me improve English writing and speaking skills. She is a good colleague, instructor and friend to me.

I also want to give my thanks to our CTC group members: Sunyoung Park, Richard Ang and Xi Qin, for supporting each other and learning from each other. We have made a great team!

Many thanks to other members in lab for their helpful suggestions and encouragement.

Many thanks to my friends especially Xi Qin for bringing laughter and helping me in my study and life.

Special thanks to Guanhong Zhou who makes me a better person.

Last but not the least, my deepest gratitude is owned to my parents, who give me endless love. Thanks for their understanding and supporting of my choices.

## **Dedication**

*To this wonderful world  
To my parents who show me the world*

## Chapter 1: Introduction

Circulating tumor cells (CTCs) were first discovered in 1869 by Thomas Ashworth who described small numbers of cells in patient blood resembling the cells of the primary tumor<sup>1</sup>. The significance of CTCs is derived from the belief that they may be the precursors for the formation of secondary tumors during metastasis<sup>2</sup>. This theory is strongly supported by the demonstrated prognostic value of CTC enumeration, which correlates to progression-free survival and overall survival of patients with metastatic carcinomas<sup>3</sup>. A key limitation in the capture and analysis of CTCs is their extreme rarity in blood relative to hematological cells (as low as 1 in  $10^9$  erythrocytes and 1 in  $10^7$  leukocytes)<sup>4,5</sup>. Mature erythrocytes have distinct physical, chemical, and biological properties that allow them to be easily removed from blood. However, leukocytes share many properties in common with CTCs, leading to high levels of leukocyte contamination in many separation methods. Therefore, effective discrimination of CTCs from leukocytes is the key functional requirement of any separation process. Current CTC separation methods can be divided into two broad categories: biochemical methods and biophysical methods.

Biochemical CTC separation methods typically rely on a combination of affinity capture of cell surface antigens to enrich for potential target cells and fluorescent labeling of intracellular markers to identify the CTCs. An established system developed using this approach has been commercialized by the Veridex CellSearch<sup>®</sup> system (Raritan, NJ, USA), which has received Food and Drug Administration (FDA) approval for clinical enumeration of CTCs. The CellSearch<sup>®</sup> system initially captures candidate cells using the cell surface antigen, epithelial cell adhesion molecule (EpCAM). The captured cells are positively identified as CTCs using fluorescent staining for cytokeratins (CK, a family of intracellular proteins that forms the cytoskeleton of epithelial cells), while leukocytes are excluded by staining for CD45 (receptor-linked protein tyrosine phosphatase that is expressed on all leukocytes). A fundamental flaw with the existing biochemical approach is that a subpopulation of metastatic tumor cells are likely to undergo epithelial-to-mesenchymal transition (EMT), which is associated with a loss of expression for epithelial marker, such as EpCAM and CK<sup>6</sup>. Consequently,

the most aggressive cancer cells may actually be the least likely to be captured and identified using this technique.

Physical CTC separation methods rely on differences in the physical properties of CTCs compared to leukocytes including cell size, shape, deformability, density, electrical polarizability, and magnetic susceptibility<sup>7</sup>. These methods are label-free, and are therefore able to avoid the epithelial antigen bias of existing biochemical methods. Furthermore, since CTCs are unmodified by physical separation processes, cells isolated using these methods are compatible with a wider range of analyses, including those requiring viable cells.

Chapter 1 first presents performance metrics used to assess different CTC separation methods (Section 1.1). Section 1.2.1 reviews the biophysical and biomechanical properties of CTCs. Section 1.2.2 to 1.2.4 reviews three main label-free methods (hydrodynamic chromatography, dielectrophoresis and filtration) in separating CTC from blood. Section 1.2.5 reviews post separation analysis and requirements for samples. Finally, Section 1.3 introduces the microfluidic ratchet mechanism for deformability based cell separation, while Section 1.4 presents the goals of the thesis.

## **1.1 Performance Metrics**

The objective of a label-free separation technology is to enrich the concentration of CTCs from an input sample to an output sample (Figure 1.1). Key performance metrics for evaluating these separation technologies include yield (also known as recovery rate or capture efficiency), depletion ratio of background cells, purity, enrichment, viability of system and throughput. Yield is the fraction of captured target cells relative to the number of target cells in the original sample (Equation 1.1). Yield is important for CTC enumeration where it is important to know the CTC concentration in the patient bloodstream. Depletion ratio of background cells is the fraction of background cells (leukocytes and erythrocytes) depleted by the device (Equation 1.2). This parameter indicates how many background cells will be retained in the output sample. Purity of the output sample is the fraction of target cells relative to the total captured cells (Equation 1.3). Purity can vary considerably depending on the concentration of CTCs in the patient's blood or the construction of the model

samples (e.g. sample doping ratio). Purity is an important metric for certain types of post-separation analysis, such as genomic profiling, but has been poorly reported in literature. Enrichment is the enhancement of the target cell to background cell ratio at the input of a separation system to the output (Equation 1.4 (A)). It can also be calculated from the yield and ratio of background cells removed (Equation 1.4 (B)). This parameter provides a single value, combining both yield and purity, that is indicative of the selectivity of a separation process. High viability is the key advantage of label-free methods over biochemical methods. Viability of a device is defined as viability of the output sample divided by viability of the input sample (Equation 1.5). Throughput indicates the speed at which the system can process a sample. This parameter is typically reported as either the volumetric flow rate or the number of cells processed per time. The number of cells processed per time is more useful since it is independent of the sample concentration.

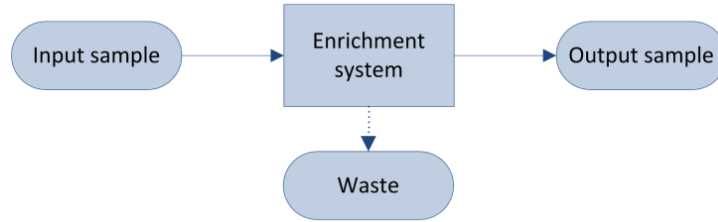


**Figure 1.1 Conceptual schematic of a cell separation system.**

$$\text{Yield} = \frac{\text{Target Cells}_{\text{output}}}{\text{Target Cells}_{\text{input}}} \quad (1.1)$$

$$\text{Depletion Ratio of Background Cells} = 1 - \frac{\text{Background Cells}_{\text{output}}}{\text{Background Cells}_{\text{input}}} \quad (1.2)$$

$$\text{Purity} = \left( \frac{\text{Target Cells}}{\text{Target Cells} + \text{Background Cells}} \right)_{\text{output}} \quad (1.3)$$

$$\text{Enrichment} = \frac{(\text{Target Cells}/\text{Background Cells})_{\text{output}}}{(\text{Target Cells}/\text{Background Cells})_{\text{input}}} \quad (1.4 \text{ (A)})$$

$$\text{Enrichment} = \frac{\text{Yield}}{\text{Background Cells}_{\text{output}}/\text{Background Cells}_{\text{input}}} \quad (1.4 \text{ (B)})$$

$$\text{Viability of System} = \frac{\text{Viability}_{\text{output}}}{\text{Viability}_{\text{input}}} \quad (1.5)$$

## 1.2 Literature Review

### 1.2.1 Biophysical and Biomechanical Properties of CTCs

Historically, CTCs were found by microscopic examination of the blood from metastatic cancer patients. When they were first identified by Thomas Ashworth in 1869, he noted that they resembled the cells of the original tumor<sup>1</sup>. In the following century there were a handful of studies which reported the observation of unusual cells in the blood of cancer patients which may have been malignant<sup>8-11</sup>. However it wasn't until the Papanicolaou stain came into widespread use in the 1950s that CTCs could be identified with greater certainty. In these studies, erythrocytes were depleted either through lysis or centrifugation, while the remaining cells were fixed and stained on a slide. Identification of CTCs was done by trained cytologists who looked for cells with features such as lobulated, crenelated, or elongated nuclei, and fragmentation or granulation of the chromatin according to Papanicolaou's criteria for malignancy<sup>12-15</sup>. In 1959 S.H. Seal observed that in density gradient centrifugation the specific gravity of CTCs appeared to be 1.065, whereas the specific gravity of leukocytes was found to be 1.056. While this difference could potentially enable separation based on this method, he also recognized the potential for significant variability in these values because of the inherent heterogeneity in both CTCs and leukocytes. He further concluded that CTCs are generally larger than other cellular elements of the blood and that they also appear to be more rigid<sup>16</sup>. Shortly after, some studies identified other large benign cells in the blood, such as megakaryocytes, macrophages and endothelial cells which may have been mistakenly identified as CTCs in previous studies<sup>17,18</sup>. The positive identification of CTCs involved examining cells from the primary tumor using the same staining technique and finding cells in the blood which were similar while being sufficiently different from any other benign cells to the eye of a trained cytologist<sup>17</sup>. Additionally, several studies noted that many CTCs were found in clusters rather than individually<sup>17-20</sup>. These historical studies demonstrated that CTCs differ from leukocytes in size, density, internal structure, as well as their tendency to form clusters – all of which could be harnessed for label-free

separation.

Recently, automated microscopy and image analysis of large numbers of fluorescently stained cells has provided additional insight into the morphology of CTCs<sup>21</sup>. In a study of CTCs from a patient with breast cancer Marrinucci et al. found CTCs to be highly heterogeneous including both high and low nuclear to cytoplasmic ratios (N/C, defined as the ratio of nuclear area and cell area with the nuclear area subtracted) and significant variation in size<sup>22</sup>. Recent findings from our group in a study of prostate cancer patients also revealed that their CTCs have significant shape variability with many having an elongated shape<sup>23</sup>. Examples of CTCs in clusters or with irregular shapes were also shown by Allard et al. in a study of 964 patients having different cancer types<sup>4</sup>. Hyun et al. compared CTCs from breast cancer patients with leukocytes, and concluded that CTCs were generally larger or of similar size to leukocytes<sup>24</sup>. Similarly, in a study of a single patient with lung adenocarcinoma, Marrinucci et al, reported that CTCs were typically larger than blood cells<sup>25</sup>. In fact, one of the historical criteria used to identify a CTC until recently was that it be larger than leukocytes<sup>26</sup>. However, this criterion is not uniformly true since CTCs <4  $\mu\text{m}$  in diameter have been discovered using the CellSearch<sup>®</sup> system<sup>4</sup>. Marinnucci et al. also discovered CTCs of the same size or smaller than leukocytes in a study of a small number of colorectal cancer patients<sup>27</sup>. Our group recently measured the average diameter of CTCs from patients with castrate resistant prostate cancer and found the average size ranged from 7.05  $\mu\text{m}$  to 8.94  $\mu\text{m}$  across different patients<sup>28</sup>. In comparison, recent measurements show various leukocyte types have typical average diameters ranging from 6~9  $\mu\text{m}$ <sup>29</sup>. These studies suggest that although many CTCs are larger than leukocytes, there is significant overlap in the size of CTCs and leukocytes that may hinder size-based separation efforts.

Deformability is likely to be an important property of CTCs in cell separations, however there is currently no data on the deformability of patient-derived CTCs due to the fact that isolated CTCs are typically fixed and stained in order to be identified, resulting in a loss of viability. However, deformability can be inferred from the nuclear to cytoplasmic ratio (N/C), where cells having larger N/C are likely to be less deformable. In a study of 36 breast cancer patients, Meng et al. observed that

the average N/C ratio of CTCs was 4.0. In contrast, they reported the N/C ratio of leukocytes to be 1.22<sup>26</sup>. Our recent study on prostate cancer patients found the average N/C ratio of CTCs to be 1.43 with significant variability<sup>28</sup>. Since the viscosity of the cell nucleus is 3~4 times greater than the cytoplasm<sup>30</sup>, CTCs are likely to be more rigid than leukocytes. To estimate the deformability differences between CTCs and leukocytes, some studies measured the deformability of cultured cancer cells<sup>31,32</sup>, or cells from the primary tumor as models<sup>33,34</sup>. Expectedly, these cells were found to be less deformable than leukocytes, typically by an order of magnitude or more. The combination of greater N/C ratio and the decreased deformability of cultured cancer cells suggests that CTCs are likely to be significantly stiffer than leukocytes, and therefore can potentially be separated using label-free processes that discriminate these cells based on deformability.

### **1.2.2 Hydrodynamic Chromatography**

Hydrodynamic separation uses interactions between particles and obstacles in flow in order to impart different flow velocities to different particles based on differences in size, and in some cases, deformability<sup>35</sup>. A key advantage of this approach over other microfluidic mechanism is its relatively high throughput (up to 600 ml/hour)<sup>36</sup>. Hydrodynamic chromatography has been applied in two different ways. The first operates in the low Reynolds number ( $R \ll 1$ ) regime where inertial effects can be ignored, while the second operates with Reynolds numbers on the order of 1 where inertial effects play an important role<sup>37</sup>. One prominent design in the low Reynolds number regime is deterministic lateral displacement (DLD) where cells below a critical size will follow streamlines and pass through an array of posts with no net lateral displacement, while the cells above a critical size will be shifted to a different streamline when they are confronted with obstructions and are laterally displaced from the original streamline<sup>38</sup>. The lateral displacement of cells is determined by the geometry of the post array, and the shape and size of each cell. This method has been shown to be capable of separating ~1  $\mu\text{m}$  diameter microparticles with a resolution of less than 20 nm<sup>39</sup>. Liu et al. separated spiked cancer cells from blood with >80% yield using DLD, demonstrating its potential for the separation of CTCs<sup>40</sup>.

The second type of hydrodynamic separation is based on inertial effects<sup>24,41-45</sup>. Recent studies have shown that in the modest Reynolds number regime between Stokes flow and inviscid flow, where both inertia and viscosity are finite, forces arising from inertial effects including drag forces from Dean flows, shear gradient lift forces, and wall-effect lift forces can be balanced against each other to enable size based separation<sup>37</sup>. Specifically, shear gradient lift force acts along the shear gradient and reaches zero at the channel centerline. The wall-effect lift force, generated by a velocity change in the fluid as it passes through the area between the particle and the wall, act orthogonal to the wall surface. In a straight channel, inertial lift forces and drag forces act orthogonally on a particle (Figure 1.2). However, in a curved channel, secondary cross-sectional flows known as Dean flows will develop due to velocity difference between the fluid in the center and near-wall regions of a channel. Dean flow will cause a particle to experience a drag force along the same axis as the shear gradient and wall-effect lift forces, all of which are orthogonal to the direction of the primary flow<sup>46</sup>. The balance of these forces results in different equilibrium positions for particles of different sizes. In the single spiral design of Bhagat et al., these inertial forces generated by the spiral microchannel geometry cause cancer cells to occupy a single equilibrium position near the inner microchannel wall<sup>47</sup>. Smaller particles (blood cells) migrate to the outer half of the channel under the influence of Dean forces resulting in the formation of two distinct particle streams which are collected in two separate outputs<sup>47</sup>. Sun et al. modified the single spiral micro-channel to create a double spiral which provides better focusing behavior of small blood cells, thus increasing yield (88.5%) and throughput ( $2 \times 10^9$  cells per hour)<sup>41</sup>. Hydrodynamic methods can typically achieve greater throughput than filtration methods, however enrichment is often poorer (<100 over leukocytes in many cases<sup>24,40,41,44</sup>) when compared with filtration methods because of its current inability to discriminate nucleated cells based on deformability.

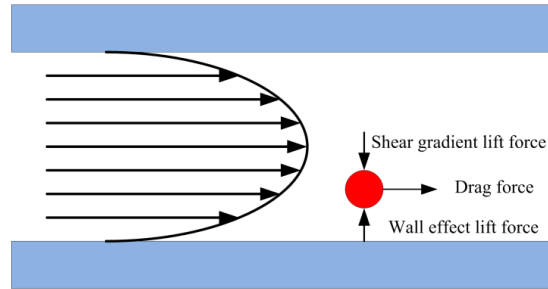


**Figure 1.2 Forces acting on a particle in a straight microchannel. Shear gradient lift force and wall-effect lift force are orthogonal to the direction of primary flow. Drag force is in the direction of primary flow and will be zero when the particle's velocity equals the flow velocity.**

### 1.2.3 Dielectrophoresis

Dielectrophoresis (DEP) is capable of discriminating between blood cells and tumor cells on the basis of cell size, nuclear morphology, and membrane morphology, all of which contribute to differences in cell membrane area and cell dielectric properties<sup>48,49</sup>. When a cell is suspended in a medium with dielectric properties distinct from the cell and is subjected to an electric field, a dipole moment along the direction of the applied field will be generated due to charges induced at the interfaces. If the electrical polarizability of the cells exceeds that of the suspending medium, the DEP force will be along the same direction as the gradient of the electric field (Figure 1.3 (A)). In this case, cells move toward the strong electric field region, resulting in positive dielectrophoresis (pDEP) (Figure 1.3 (B)). On the other hand, when the electrical polarizability of the cells is less than that of the medium, the direction of the DEP force acts in the reverse direction (Figure 1.3 (C)) and cells move to the weak electric field region, resulting in negative dielectrophoresis (nDEP) (Figure 1.3 (D))<sup>50</sup>. The polarizability of a cell depends strongly on its composition, morphology, and the frequency of the applied electric field<sup>51</sup>. Therefore, cells of different phenotypes or physiological states can potentially be discriminated using this approach<sup>48</sup>.

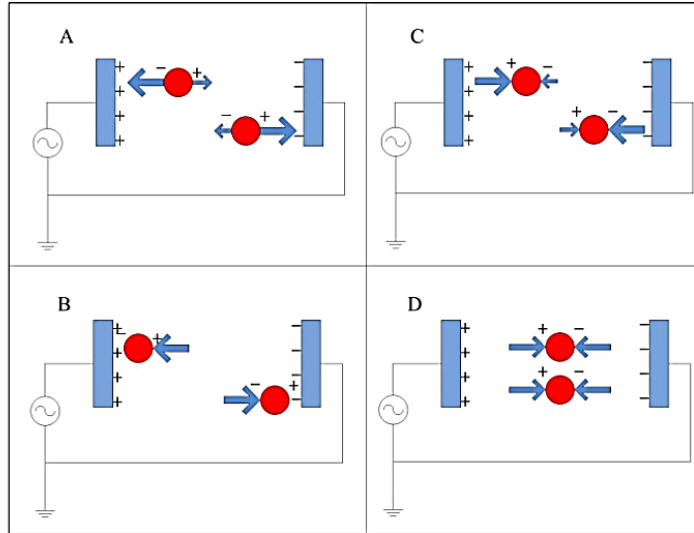


**Figure 1.3 Dielectrophoresis: (A) Positive DEP; (B) Particle equilibrium point in pDEP; (C) Negative DEP; (D) Particle equilibrium point in nDEP.**

Using DEP, Alazzam et al. demonstrated the separation of cultured cancer cells from blood with 96% yield<sup>52</sup>. Gascoyne et al. used DEP to separate mixtures of three different cultured tumor cell types doped into peripheral blood with >90% yield<sup>53</sup>. Additionally, Gascoyne et al. also found correlations between the dielectric properties of cells and their exterior morphology, which may provide a basis for predicting the DEP behavior of CTCs<sup>29</sup>. Recently, DEP cell separation has been improved by combining DEP with other separation techniques. Shim et al. designed a system with a continuous flow microfluidic processing chamber, whereas previous microfluidic DEP methods processed the sample in batches. Similar research has been conducted by Moon et al.<sup>54</sup> who combined multi-orifice flow fractionation (MOFF) and dielectrophoresis together to enrich the concentration of MCF-7 cells 162-fold over erythrocytes at a 7.6 ml/hour flow rate<sup>55</sup>. Compared to filtration and hydrodynamic methods, DEP-based methods currently lag in performance in both selectivity (enrichment over leukocytes typically <100) and throughput (typically <1 ml/hour).

#### 1.2.4 Filtration

Filtration is the process of flowing a cell sample through an array of micro-scale constrictions in order to capture target cells based on a combination of size and deformability. Filtration microstructures developed for the separation of CTCs can be categorized into three basic types:

weir<sup>56-58</sup>, pillar<sup>59-61</sup>, and pore<sup>62-64</sup>. Weir structures consist of microchannels containing a sudden decrease in the channel cross-section (Figure 1.4 (A)). Pillar structures consist of an array of micro-posts spaced appropriately to form constrictions to capture target cells (Figure 1.4 (B)). Pore structures consist of a membrane perforated with a 2D array of small holes (Figure 1.4 (C)). The key design parameters in these filter microstructures include the flow rate of the fluid and the cross-sectional opening of the constrictions. The fluid flow rate determines the force applied to each cell as it is deformed through a constriction. The cross-sectional opening determines the size and shape of the deformed cell that can be captured by the filter. The combination of the two therefore determines the threshold size and deformability of target cells that can be caught by the filter. The practical limit of this process is the maximum force that can be tolerated by the filtered cells before causing permanent damage<sup>65</sup>. Cancer cells and other large cells in blood were captured by Seal in 1964 by pore type filtration using a perforated section of clear plastic tape<sup>66</sup>. Vona et al. also characterized this method using pores in a polycarbonate membrane to capture cultured tumor cells spiked into peripheral blood and succeed in detecting a single tumor cell added to 1ml of blood<sup>67</sup>. Recent devices developed using this principle have demonstrated the ability to capture >85% doped cultured cancer cells in work by Lin et al.<sup>62</sup>, Lu et al.<sup>61</sup>, Zheng et al.<sup>64</sup>, McFaul et al.<sup>59</sup>, and Lin et al.<sup>68</sup>. Among them, Lin et al.<sup>62</sup>, Zheng et al.<sup>64</sup>, and Lin et al.<sup>68</sup> have demonstrated the ability to enrich the population of doped cancer cells by a factor of >1000. Several commercial devices utilizing the pore structure concept have also been introduced, including the Rarecells®<sup>69</sup>, ScreenCell®<sup>70</sup>, and ClearCell®<sup>60</sup> devices. Studies of the effectiveness and clinical utility of these devices are currently ongoing<sup>71-74</sup>.

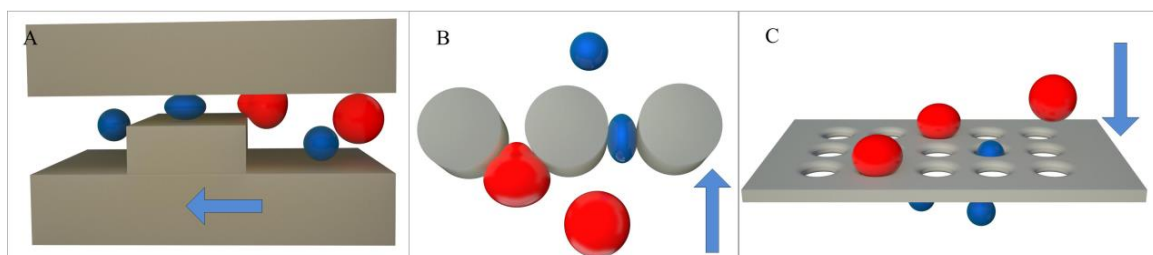


**Figure 1.4 Filtration mechanisms: (A) Weir, (B) Pillar, (C) Pore.**

One of the key challenges in using mechanical constrictions to separate CTCs is the potential for clogging when large numbers of cells are processed, which can cause unpredictable variations in flow rate and consequently in the force applied to squeeze cells through each constriction. McFaul et al. addressed this shortcoming by periodically clearing the filter element with an oscillatory flow<sup>59</sup>.

### 1.2.5 Post-separation Analysis

Post-separation analysis of CTCs includes identification, enumeration, and characterization. Currently, the widely accepted definition of CTCs involves the expression of epithelial markers (EpCAM, cytokeratins) and the absence of the leukocyte marker CD45<sup>75</sup>. Additionally, CTCs can also be defined based on the expression of stem cell markers (e.g. CD133), mesenchymal markers (e.g. vimentin), or the shift in expression from epithelial E-cadherin to mesenchymal N-cadherin<sup>76,77</sup>. Identification of CTCs via these markers can be performed using immunofluorescence, which is tolerant to contaminants in the output cell sample, as demonstrated in work by Nieva et al.<sup>78</sup> and Marrinucci et al.<sup>22,79</sup>. Therefore, for the purpose of CTC enumeration, the key performance parameters for label-free separation technologies are yield and throughput. Since CTC concentration is extremely low in the bloodstream, the enrichment of the separation system still needs to be high enough such that the target CTCs can be microscopically examined and distinguished from background cells in a reasonable amount of time.

A defining feature of CTCs is the genetic instability derived from the primary tumor. Fluorescent *in-situ* hybridization (FISH) of labelled DNA probes can be used to assess genomic instability and has been employed in the assessment of the status of the human epidermal growth factor receptor 2 (HER2), that is commonly overexpressed in breast and prostate cancer CTCs<sup>80,81</sup>. Similar to immunofluorescence, FISH is tolerant of cellular impurity but requires a high capture rate. Genetic instability can also be assessed by direct genomic profiling. Array-comparative genomic hybridization can assess genomic status of CTCs to infer the genomic profile of the primary tumor<sup>82</sup>. Similarly, polymerase chain reaction (PCR)-based methods can be employed to amplify tumor-specific abnormalities present in the DNA or mRNA. Conventional PCR, nested PCR and

quantitative real-time (qRT)-PCR can be used for both qualitative and quantitative measurement of the expression level of the specific target sequence. This method requires high quality nucleic acid as a template, which necessitates a nucleic acid purification step after separation. The specific and qualified primers and the appropriate control reference are of great importance for this detection method. PCR-based approaches have the advantage of being very sensitive with the lower limit of reliable detection currently at a concentration of 0.7 cells/ml<sup>83</sup>, but with the disadvantage of low specificity due to even minimal contamination.

Similarly, overexpression of cancer-associated genes can be assessed by analysis of the protein or expressed RNA of captured CTCs. Enzyme-linked immunosorbent assay (ELISA) can be employed to examine protein overexpression but requires a high capture efficiency and sample cell purity because ELISA has limited sensitivity. On the other hand, polymerase chain reaction (PCR)-based methods are much more widely used for detecting overexpression of cancer-associated genes. Devriese et al. use polymerase chain reaction with a panel of marker genes expressing cytokeratin 7 and 19, human epithelial glycoprotein and fibronectin 1 after immunomagnetic bead enrichment was performed. Then they use quadratic discriminant analysis to indicate CTC-positivity or CTC-negativity<sup>84</sup>. Reverse transcriptase-polymerase chain reaction (RT-PCR) based assays detect tissue-specific mRNAs in peripheral blood, and thus their specificity for tumor cells depends on the assumption that normal tissue cells do not circulate, unless they become tumorous<sup>67</sup>. Louha et al. showed that liver resection and needle liver biopsy will induce a release of cells from the liver into peripheral blood circulation<sup>85</sup>. Therefore, although RT-PCR has high sensitivity, it may not be suitable for characterizing CTCs in cell preparations with a high number of contaminating non-target cells. Another detection method combines PCR and ELISA together, using PCR products as the specific probe for ELISA quantification<sup>86</sup>. This technique has a higher sensitivity level than standard RT-PCR. PCR based approaches are sufficiently sensitive to have been proposed for characterization of circulating tumor DNA from cell-free plasma preparations<sup>87</sup>. However, this circulating DNA would have a significant degree of DNA impurity from non-CTC cells and the capacity to capture CTCs would minimize the impact of non-target contamination.

Another approach to the characterization of CTCs is to quantify their biophysical and biomechanical properties including size, morphology, and deformability<sup>88</sup>. Methods of characterization include visual microscopy<sup>21,22</sup>, AFM<sup>33,89</sup>, micropipette aspiration<sup>31,34</sup>, electrical stretching<sup>90,91</sup>, and optical tweezers<sup>92,93</sup>. Since these characterization processes are typically applied on single cells, a relatively pure cell sample is required. Furthermore, since cell deformability is influenced by cell death, as well as physical and chemical damage, the capture of viable cells is a requirement for these types of studies.

In summary, the required specifications of CTC separation technologies depend critically on the desired post-separation analysis as shown in Table 1.1. For enumeration, yield is the most important parameter, but enrichment should also be high enough that all the cells in the output sample can be examined in a reasonable amount of time. Characterization processes such as genomic profiling require CTC purity in the output sample to be as high as possible. For example with a starting ratio of CTCs to leukocytes as low as 1:10<sup>7</sup> in the bloodstream<sup>5</sup>, the initial sample will need to be enriched  $>2.33 \times 10^7$  to reach a sample with a CTC purity of 70%. Such demanding performance specifications suggest that multiple separation technologies will likely be needed to obtain the required purity.

**Table 1.1 Post-separation analysis and requirements.**

<b>Methods</b>	<b>Applications</b>	<b>Most important sample requirement</b>
<b>Immunofluorescence</b>	Enumeration and detection	Yield
<b>FISH</b>	Characterization and detection	Yield
<b>Genomic profiling and DNA sequencing</b>	Characterization of genomic instability and relevant mutation.	Purity
<b>Gene expression and transcription profiling</b>	Characterization of tumor marker overexpression	Purity
<b>PCR</b>	Characterization of tumor marker overexpression	Purity
<b>ELISA</b>	Characterization of tumor marker overexpression	Yield and Purity
<b>Deformability measurement</b>	Biomechanical characterization	Viability
<b>Size and morphology analysis</b>	Biomechanical characterization	Yield

### 1.3 Microfluidic Ratchet Mechanism for Deformability based Cell Separation

A microscale ratchet mechanism where the local asymmetry is coupled to the deformability of individual cells through microscale funnel constrictions has been demonstrated by Guo et al.<sup>94</sup>. The threshold pressure to transport single cells through these constrictions along the direction of the taper is smaller than against the taper (Figure 1.5). This asymmetrical deformation force can enable selective and irreversible transport of individual cells when a square wave oscillation pressure is applied. Our previous studies have proven that the microscale funnel matrix can be used for deformability based cell sorting and ratchet mechanism based platforms have higher selectivity compared to other label-free methods<sup>59,95</sup>. However, the batch processing mode in our previous studies results in very low throughput which limits further CTC enumeration from patient samples.

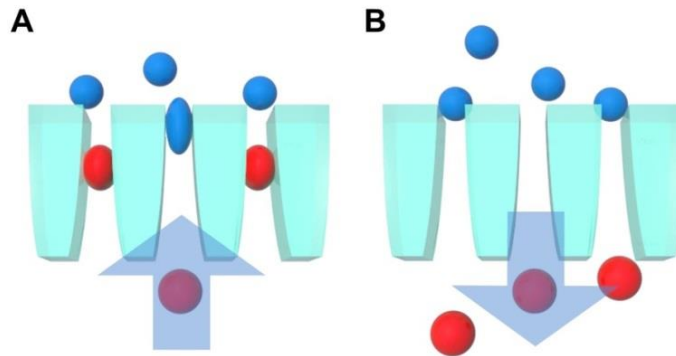


**Figure 1.5 Microfluidic ratchet: Large stiff cells are prevented from transiting through the pores in forward flow (A) while smaller more deformable cells are prevented from returning under reverse flow (B).**

### 1.4 Goals of the Thesis

In this study, our goal is to develop a microfluidic device for deformability-based separation of circulating tumor cells from whole blood samples based on the microfluidic ratchet mechanism. Specifically, we aim to:

- Devise an improved mechanism for continuous cell separation using the microfluidic ratchet mechanism;
- Characterize the separation system performance using cultured cancer cells as model;
- Separate and detect CTCs from blood samples obtained from patients with Castration-Resistant Prostate Cancer (CRPC).

## Chapter 2: Microfluidic Ratchet Mechanism for Cell Separation

This chapter describes the motivation and design of the microfluidic ratchet mechanism for deformability-based cell separation. Section 2.1 describes how clogging degrades selectivity in traditional filtration system. Section 2.2 describes the microfluidic ratchet mechanism and how it can be used for cell separation without clogging. Section 2.3 describes continuous cell separation using the microfluidic ratchet mechanism.

### 2.1 Clogging in Traditional Filtration System

One of the key problems in using traditional filtration methods to separate cells is clogging whereby cells accumulated in the filter pores (Figure 2.1 (A)) modify the hydrodynamic resistance of the filter in an unpredictable way (Figure 2.1 (B)). As a result, the flow rate through the remaining vacant pores is varied in an unpredictable way, which results in an uncertainty in the filtration force imparted to the cells. The selectivity of these filtration methods will be degraded by cell accumulation as sample is processed. Additionally, since the sample is flowed through the filter in one direction, it is very difficult to remove cells trapped by the filter in the separation process.

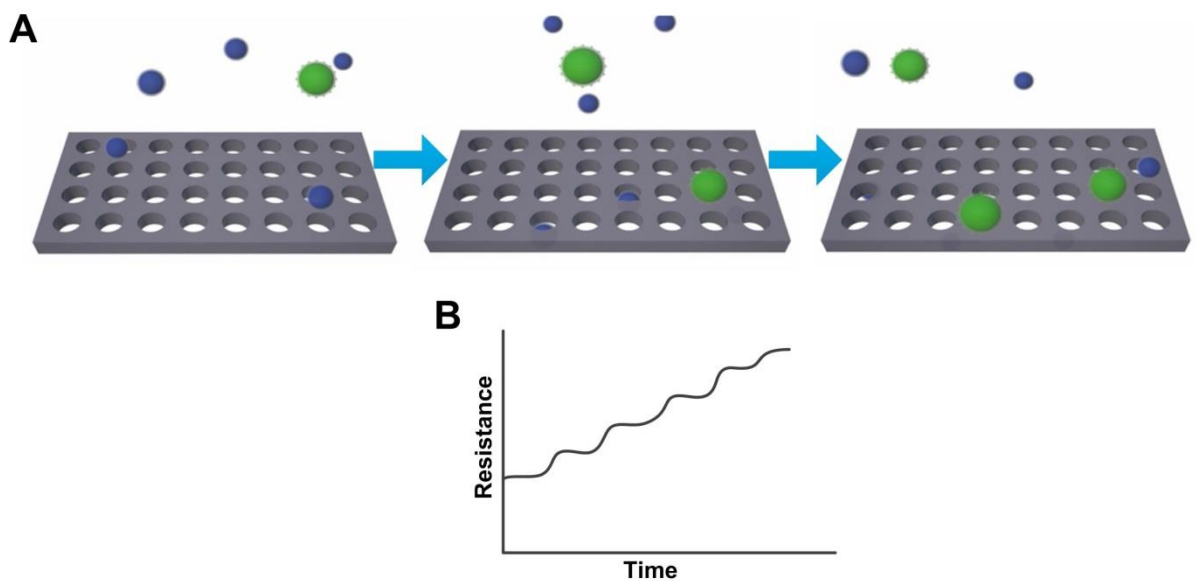


**Figure 2.1 Working principle of a traditional membrane filter (A) and how the resistance changes as process time goes by (B).**

To solve this problem, there should be two directions of flow, one for filtration, one for retrieving cells and clearing pores. However, for a simple membrane filter, cells having passed through pores will typically come back during reverse flow because of the reversibility of low-Reynolds number flow. To address this issue, my research group developed the microscale ratchet mechanism that requires greater reverse pressure to transport cells back to replace regular pores. In this scheme, captured cells can be retrieved and funnels are cleared for other cells to be sorted, while background cells that have gone through the funnels will not be retrieved. At the same time, resistance of filter will remain constant and flow through funnels will be stable.

## **2.2 Microfluidic Ratchet Mechanism**

### **2.2.1 Physical Asymmetry of Ratchet Mechanism**

Our group has previously presented a microscale ratchet mechanism where the local asymmetry is coupled to the deformability of individual cells through microscale funnel constrictions<sup>94</sup>. The microfluidic ratchet mechanism can be applied for cell sorting based on deformability. Deformability refers to the ability to change shape under a given level of applied stress. It is more distinguishable among different types of cells because it is related to the composition of cytoplasm, the structure of the cytoskeleton, and nucleus-cytoplasm ratio. To better understand the deformation of cells through micrometer scale constrictions, we modeled cells as a Newtonian liquid droplet enclosed by a cortical layer with a constant and isotropic tension,  $T_0$ . Cell surface microvilli were neglected in the current model by assuming a smooth membrane surface. We further assume that fluid surrounding the cell membrane and fluid enclosed by the cell membrane are homogeneous and incompressible, which implies a spherical geometry of cells in suspension<sup>96</sup>. As a cell deforms through a constriction with a rectangular cross-section as shown in Figure 2.2 and Figure 2.3, the internal pressure of the cell is denoted  $P_{int}$  while  $P_1$  and  $P_2$  are the pressures acting on the leading and trailing membranes of the cell respectively.

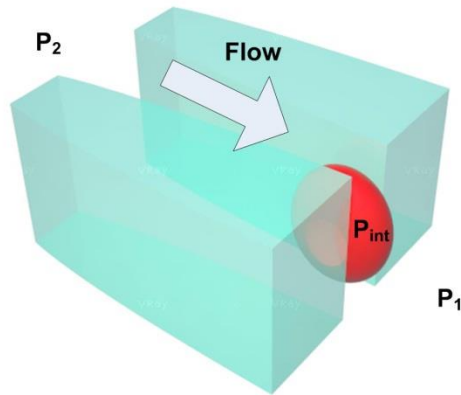


**Figure 2.2** Three dimensional view of a cell deforming through a funnel constriction. the internal pressure of the cell is denoted  $P_{int}$  while  $P_1$  and  $P_2$  are the pressures acting on the leading and trailing membranes of the cell respectively.

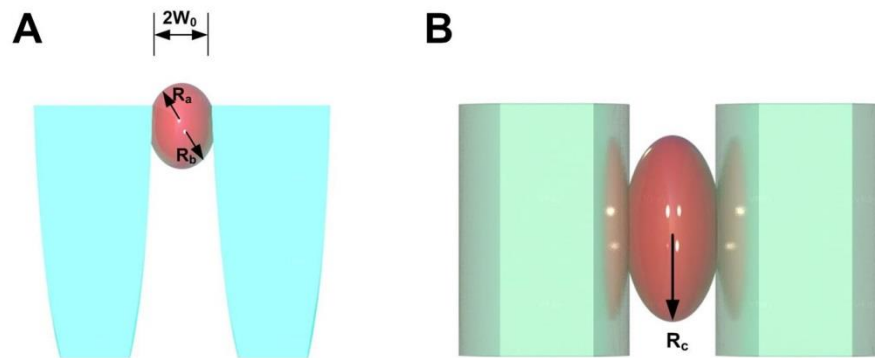


**Figure 2.3** Top view (A) and front view (B) of a cell deforming through a funnel.

The balance of forces acting on both membranes is analyzed as follows (Figure 2.4). Both membranes have two radii of curvature, one constrained by the geometry of the funnel, and the other is not. The constrained radius is denoted  $R_a$  and  $R_b$  for leading and trailing membranes of the cell respectively. The unconstrained radius is denoted  $R_{c1}$  and  $R_{c2}$  respectively.

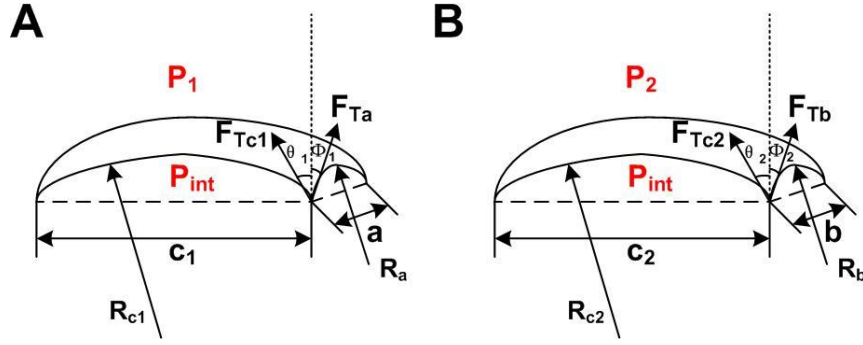


**Figure 2.4 Schematic of forces acting on a curved membrane. (A) Leading edge membrane. (B) Trailing edge membrane.**

In the case of leading edge, the normal components of membrane tension forces,  $F_{c1}$  and  $F_a$ , are equal to the force from the pressure difference on either side of the membrane:

$$(P_1 - P_{int}) \times a \times c_1 = F_{c1} \cos \theta_1 + F_a \cos \phi_1 \quad (2.1)$$

The membrane tension forces are defined as the cortical tension times by the length of the membrane edges over which they act, such that:

$$F_{c1} = T_0(2a) \quad (2.2)$$

$$F_a = T_0(2c_1) \quad (2.3)$$

Substituting these tension force terms into Equation 2.1 yields:

$$(P_1 - P_{int}) \times a \times c_1 = 2T_0(ac \cos \theta_1 + c_1 \cos \phi_1) \quad (2.4)$$

Furthermore, by geometry:

$$\cos \theta_1 = \frac{c_1}{2R_{c1}} \quad (2.5)$$

$$\cos \phi_1 = \frac{a}{2R_a} \quad (2.6)$$

Substituting Equation 2.5 and 2.6 into Equation 2.4, and dividing by a factor of  $ac_1$  gives:

$$P_1 - P_{int} = T_0 \left( \frac{1}{R_{c1}} + \frac{1}{R_a} \right) \quad (2.7)$$

For the trailing edge membrane:

$$P_2 - P_{int} = T_0 \left( \frac{1}{R_{c2}} + \frac{1}{R_b} \right) \quad (2.8)$$

To find the expression for the applied pressure on the entire cell, we can subtract Equation 2.7 from Equation 2.8 thus eliminating  $P_{int}$ :

$$P_1 - P_2 = T_0 \left( \frac{1}{R_{c1}} + \frac{1}{R_a} - \frac{1}{R_{c2}} - \frac{1}{R_b} \right) \quad (2.9)$$

The difference between  $R_{c1}$  and  $R_{c2}$  is considered small enough to be negligible. This reduces Equation 2.9 to the following form:

$$\Delta P = T_0 \left( \frac{1}{R_a} - \frac{1}{R_b} \right) \quad (2.10)$$

As the leading edge of the cell is pulled into the constriction,  $\Delta P$  eventually reaches a maximum and then decreases upon further deformation. This phenomenon causes an instability known as a Haines jump, whereby the entire cell is pulled rapidly through the microstructure<sup>97</sup>.

When cell is deformed in the backward directions through the funnel (Figure 2.5),  $R_b$  is much bigger than  $R_a$ , which means higher pressure difference is needed to push the cell through the funnel compared to forward flow. This asymmetrical deformation force can enable selective and irreversible transport of individual cells when a square wave oscillation pressure is applied.

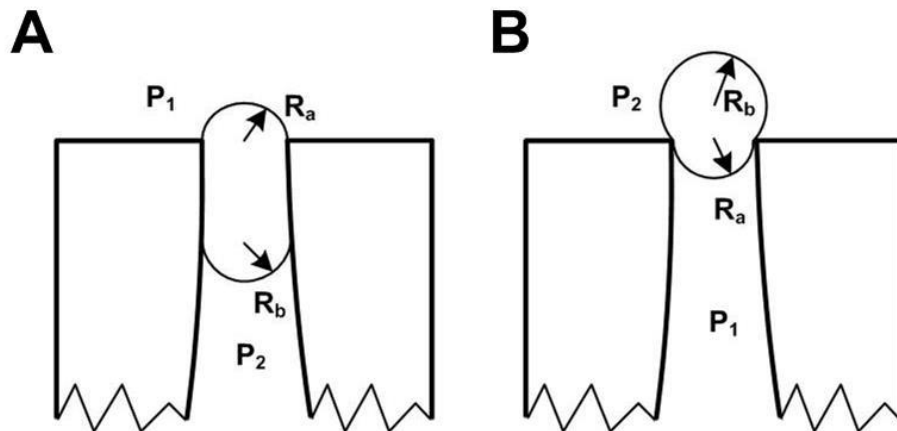


**Figure 2.5 Deformation of a single cell through microscale funnel constrictions in forward (A) and backward (B) directions.**

### **2.2.2 Cell Separation using Ratchet Mechanism**

Our previous studies have proven that the microscale ratchet matrix can be used for deformability based cell sorting when a square wave oscillation pressure is applied<sup>59,95</sup>. The microscale ratchet matrix contains multiple rows and columns of funnels. The pore size in each row is constant but the pore sizes between rows are incrementally smaller from the bottom to the top. In the original cell separation device based on the microfluidic ratchet mechanism developed by Sarah McFaul<sup>59,95</sup>, there are three steps in each separation cycle. Cells are first infused into this microscale ratchet matrix. Then forward pressure is applied for cell sorting and backward pressure is applied for clearing all funnels that clogged by cells. Because of the ratchet mechanism, cells that have deformed through the funnels will not come back when the backward pressure is applied. After subjecting the cell sample to the oscillatory flow, cells with greater deformability will transport to top rows while the cells with smaller deformability will be retained in bottom rows in this funnel matrix. Finally, cells in top rows and bottom rows will be collected in different outlets and a new batch of cells will be infused into the ratchet matrix for separation. This cell separation strategy shows higher selectivity than other filtration methods and avoids the clogging problem that degrades selectivity. However, for enumeration of CTC in blood, the system should be able to process large amount of sample (at least 1 ml whole blood which contained  $\sim 5 \times 10^6$  leukocytes) because of the rarity of CTCs in blood. The batch process developed previous did not have sufficient throughput (less than 10,000 leukocytes per hour) to handle a reasonable blood volume in practical clinical applications.

### **2.3 Continuous Cell Separation using Microfluidic Ratchets**

To increase the throughput of this mechanism, or alternatively, to increase utilization of the filtration microstructure, we developed a continuous microfluidic strategy based on the microfluidic ratchet mechanism to enable microfiltration based enrichment of viable CTCs while minimizing clogging. Specifically, the sample is injected into the bottom-left of the funnel matrix (Figure 2.6). Cells entering into the microscale funnel matrix are pushed to the right by an applied buffer pressure while simultaneously being pushed up or down by the oscillation pressure allowing them to travel diagonally up in the matrix. In this way, using an oscillating vertical pressure coupled with a constant

horizontal buffer pressure, a mixed population of cells becomes increasingly more separated as it travels to the right until each cell is retained by a pore that is too small to pass through. Erythrocytes are the smallest and most deformable cells and therefore migrate past the top row of the matrix. Leukocytes are generally smaller and more deformable than CTCs and are displaced to near the top of the funnel matrix. CTCs are retained in the bottom rows for larger size and smaller deformability. By collecting cell fractions in the bottom rows that contain cancer cells, it is possible to achieve a highly enriched population of these cells.

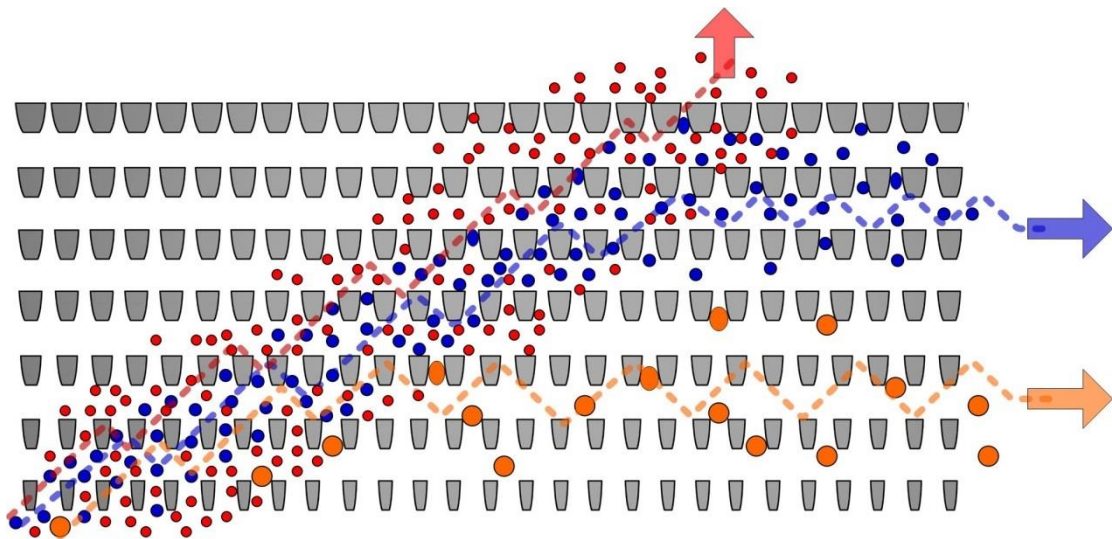


**Figure 2.6 Operation of the microfluidic ratchet mechanism. Cells are introduced into the bottom-left of the funnel matrix and travel in a step-wise diagonal path before reaching a limiting funnel size. CTCs (orange), leukocytes (blue), and erythrocytes (red) each follow a distinct path in the matrix.**

By switching the previous batch processing mode to continuous processing mode, more funnels can be utilized by the cell sample, which dramatically increases throughput. At the same time, elimination of microvalves that controls batch processing can simplify device fabrication and operation procedures. These improvements enable this device capable of processing clinical blood samples to separate and detect CTCs.

## Chapter 3: Device Design and Modeling

Section 3.1 describes the design of the cell separation device based on the microfluidic ratchet mechanism. Section 3.2 describes the system-level hydrodynamic resistance analysis. Section 3.3 and Section 3.4 describes the design and calculation of the hydrodynamic resistance of the funnel matrix and supporting channels. Finally, Section 3.5 analyzes the variation in oscillation resistance of cutoff funnels and the variation in total oscillation flow rate caused by cells that occupy the funnels.

### 3.1 Device Design

The device is composed of a central separation area and supporting elements including inlet, outlets, and oscillation microchannels for flow control (Figure 3.1). Cells are infused from the sample inlet channel and going into the sorting area from the left bottom. Buffer pressure generates a horizontal flow that enables cells transport from the left edge to the right edge. Oscillation flow is generated from the oscillation pressure inlets at the top and bottom of the device. Bifurcations in buffer channel and oscillation channels ensures even distribution of the flow. The flow rate in the channels can be adjusted by adjusting the pressure at the inlets.

The central separation area comprises a 2D array of microscale funnel constrictions. We designed a prototype first which has 32 rows by 512 columns in this constriction matrix. After characterization and test, we modified the design to a 4× extended version which has 32 rows by 2048 columns in this constriction matrix. From 1× to 4× device, the number of funnels that can be used for cell separation is enlarged to 4 times. In addition, when the same number of cells is captured in the filter, the variation in filter resistance is reduced which makes the filtration system more reliable.

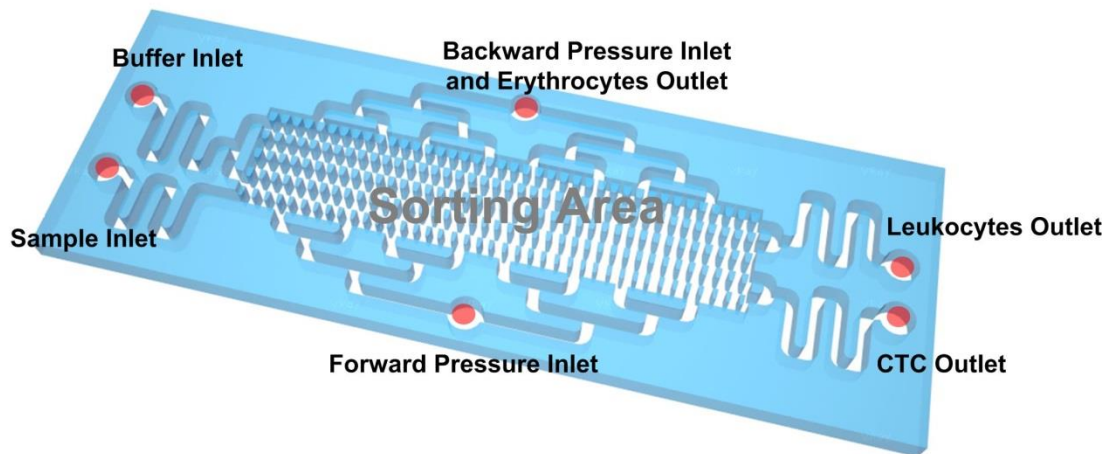


**Figure 3.1 Schematic draw of microfluidic ratchet device. The device consists of sample inlet, buffer inlet, sampler outlet, waste outlet, oscillation microchannels and central sorting area.**

The pore size in each row is constant but the pore sizes between rows are incrementally smaller, ranging from  $18\ \mu\text{m}$  to  $2\ \mu\text{m}$ . 32 rows can allow capturing more specific type of cells in further work. 2048 columns can allow more cells being sorted at the same time, thus increasing the throughput. There are 8 rows in the middle with pore size of  $6\ \mu\text{m}$  working as cutoff for separating CTCs from leukocytes. Deformability plays a less important role when pore size is larger than  $6\ \mu\text{m}$  and cells undergo excessive deformation when pore size is smaller than  $6\ \mu\text{m}$ .  $6\ \mu\text{m}$  pore size is chosen for both enrichment based separation and avoiding damage on cells. Cells that can deform through these cutoff rows are collected in the leukocyte outlet and the others below these rows are collected in the CTC outlet. The pressure difference of these cutoff funnels is the key to adjust separation performance of the device. There are a total of 8 rows of funnels at the cutoff size, which ensures that cells are sorted sufficiently and that the CTCs will not travel beyond the cutoff funnels even in collision with the leukocytes.

During processing, cells enter the funnel matrix at the bottom left and are pushed to the right by the constant pressure applied at the cell inlet and buffer inlet. During the forward flow part of the oscillation cycle, both buffer pressure from left and forward pressure from bottom push the cells to travel diagonally across the sorting area before the cells reach the funnels that is too small to deform

through (Figure 3.2 (A)). During the reverse flow part of the oscillation cycle, both buffer pressure from left and backward pressure from top push the cells to travel diagonally down, which clears the pores of any cells which may have become trapped (Figure 3.2 (B)). After backward pressure, cells are pushed diagonally up again. The magnitudes of the upward and downward pressures are the same; however the upward pressure is applied for slightly longer to give the cells a net upward displacement. A constant pressure is applied at the sample and buffer inlets to provide a constant horizontal flow through the funnel matrix.

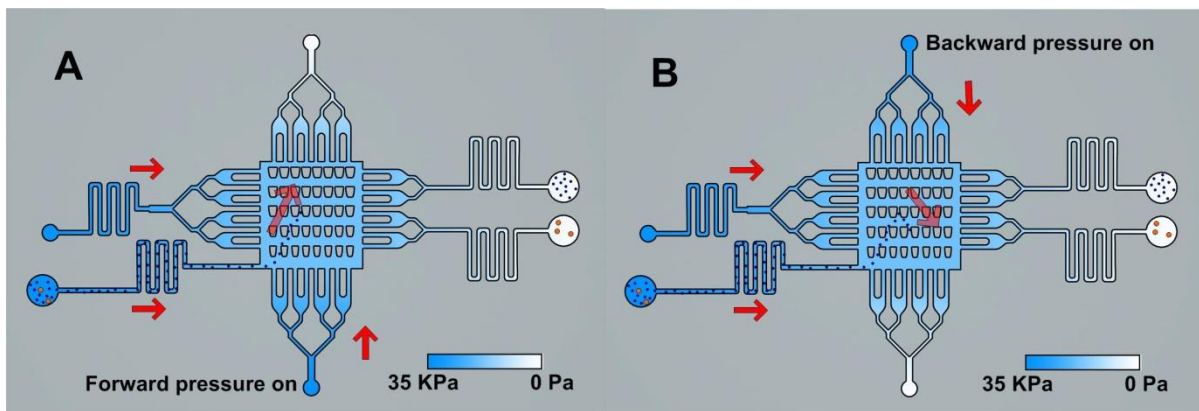


**Figure 3.2 Device operation schematic: Cells are introduced through the sample inlet to the bottom left. Inside the funnel array cells are alternately pushed forward and backward. (A) Forward flow part. (B) Backward flow part.**

### 3.2 System Hydrodynamic Resistance Analysis

Our microfluidic device can be divided into several hydrodynamic components including sample inlet channel, buffer inlet channel, oscillation channel, outlet channels and central sorting matrix (Figure 3.3). Oscillation channel resistance is denoted as  $R_{osc-c}$ . Oscillation resistance of the sorting matrix is denoted as  $R_{osc-s}$ . Buffer channel resistance is denoted as  $R_{buffer-c}$ . Buffer resistance of the sorting matrix is denoted as  $R_{buffer-s}$ . Sample inlet channel resistance is denoted as  $R_{sample}$ . Outlet channel resistance is denoted as  $R_{outlet}$ . For the hydrodynamic resistance of central sorting matrix, each funnel is simplified as oscillation resistance unit  $r_i$  (in vertical direction) and buffer resistance unit  $r_j$  (in horizontal direction).  $R_{osc-s}$  can be calculated by parallel connection and series connection of  $r_i$ . Similarly,  $R_{buffer-s}$  can be calculated by parallel connection and series connection of  $r_j$ . Specifically, they can be expressed as:

$$R_{osc-s} = \sum_{i=1}^{total\ number\ of\ rows} \frac{r_i}{total\ number\ of\ columns} \quad (3.1)$$

$$R_{buffer-s} = \frac{1}{\sum_{j=1}^{total\ number\ of\ rows} \frac{1}{r_j}} \times total\ number\ of\ columns \quad (3.2)$$

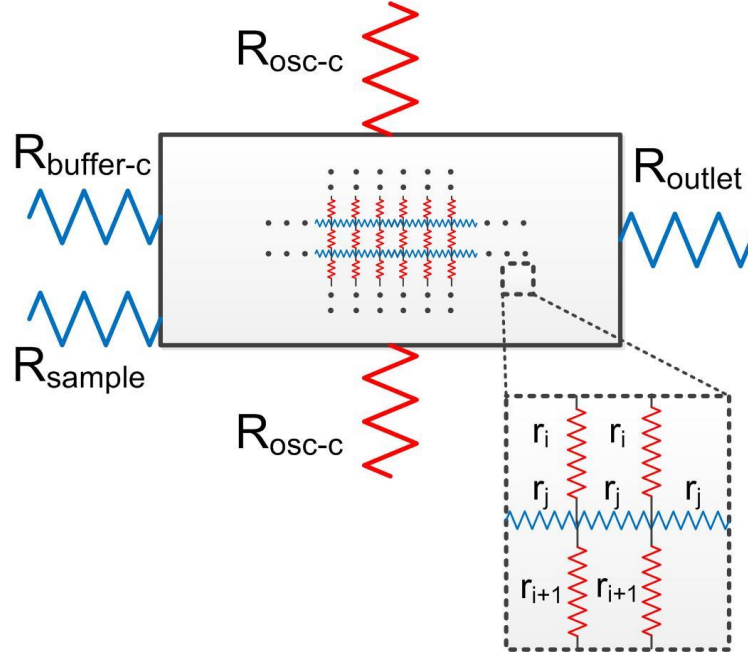


**Figure 3.3 Hydrodynamic resistance analysis of the device for flow control.**

The diagonal flow in the device can be divided into oscillation flow (in vertical direction) and buffer flow (in horizontal direction). The oscillation flow through the cutoff funnels is related to the pressure difference of cutoff funnels which is the key parameter in adjusting system performance. To make the oscillation flow more adjustable, the resistance in oscillation channels is designed to be much smaller than buffer channel resistance and outlet channel resistance. As a result, when oscillation pressure is applied alone, the dominant flow in the sorting area is oscillation flow. Because of the symmetry of the device with cutoff funnels as symmetric axis, the buffer pressure will not affect net oscillation flow rate and the oscillation flow rate in cutoff funnels. The oscillatory flow and the buffer flow are essentially independent of each other at the cutoff funnels. Therefore, only the oscillation pressure difference need to be considered when estimating the oscillatory flow rate as well

as deformation pressure applied to each cell in across the cutoff funnels. The oscillation flow rate is mainly determined by the oscillation pressure difference and total oscillation resistance (the total hydrodynamic resistance of the oscillation channels and the sorting matrix), or specifically,

$$Q_{Tosc} = \frac{\Delta P_{osc}}{R_{Tosc}} \quad (3.3)$$

The buffer flow is mainly determined by the pressure difference of buffer inlet and sample outlet, and the total resistance in buffer direction (the total hydrodynamic resistance of the buffer channel, sorting matrix, and the outlet channels), or specifically,

$$Q_{Tbuffer} = \frac{\Delta P_{buffer}}{R_{Tbuffer}} \quad (3.4)$$

The flow rate of the sample going into the device is mainly determined by the pressure at sample inlet, sample inlet channel resistance, buffer channel resistance and outlet channel resistance. The sample pressure should be balanced with buffer pressure at the left edge.

As stated in Section 2.2.1, the pressure difference of the funnels determines whether the cell can deform through the funnel or not (Equation 2.10). In the funnel ratchet matrix, the pressure difference of the cutoff funnels (Figure 3.4) is the key parameter in adjusting system performance. Higher pressure difference of the cutoff funnels allows more cells to deform through cutoff funnels which results in less contamination of background cells but lower capture efficiency of target cells. Lower pressure difference of the cutoff funnels can achieve higher capture efficiency of target cells but also high contamination of background cells because of the smaller force applied on all cells. To understand how the applied pressure difference at the oscillation inlets is related to system performance, we need to know how the applied pressure difference at the oscillation inlets will be transferred into the pressure difference at the cutoff funnels.

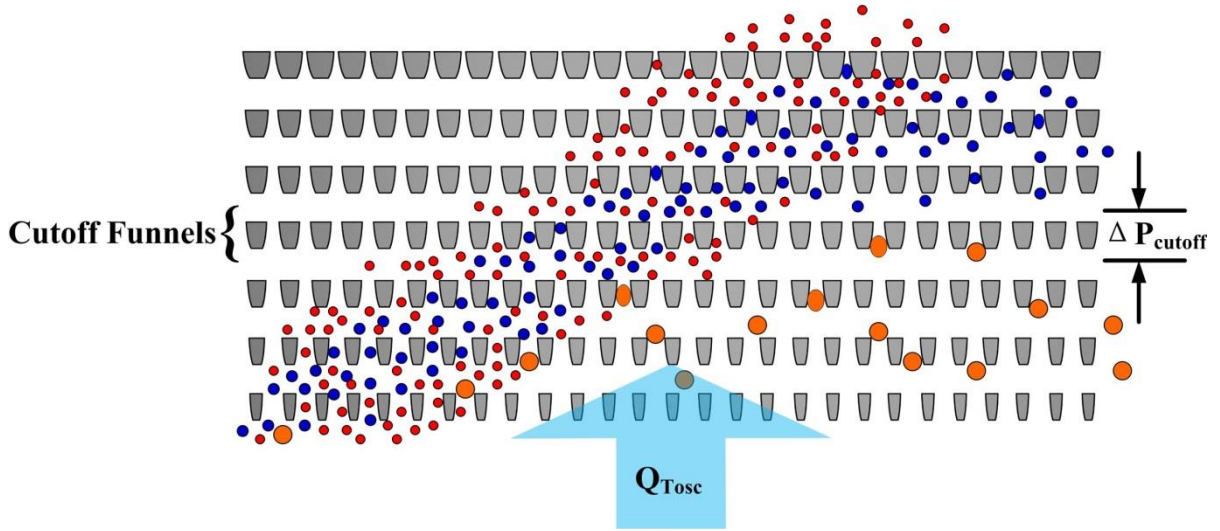


**Figure 3.4 Cutoff funnels and pressure difference of cutoff funnels.**

The pressure difference of the one row of cutoff funnels ( $\Delta P_{cutoff}$ ) can be derived by the total flow in the oscillation direction ( $Q_{Tosc}$ ) and one row cutoff funnels' total oscillation resistance ( $R_{cutoff}$ ) in the following expression:

$$\Delta P_{cutoff} = Q_{Tosc} \times R_{cutoff} \quad (3.5)$$

Where,

$$Q_{Tosc} = \frac{P_{osc}}{2 \times R_{osc-c} + R_{osc-s}} \quad (3.6)$$

To maintain a constant pressure difference across the cutoff funnels, the total flow rate in oscillation direction should also be kept constant (Equation 3.5). While the oscillation pressure ( $P_{osc}$ ) and oscillation channel resistance ( $R_{osc-c}$ ) will not change during processing, the resistance of the sorting matrix in oscillation direction ( $R_{osc-s}$ ) may change with the number of captured cells. To keep the total flow rate in oscillation direction constant, the variation in the sorting matrix's resistance in oscillation direction should be negligible. Therefore,  $R_{osc-c}$  and  $R_{osc-s}$  should have the relationship as follows:

$$R_{osc-c} \gg R_{osc-s} \quad (3.7)$$

In this case, small variation in the oscillation resistance of the sorting area can be neglected in Equation 3.6. So the pressure difference of the cutoff funnels will not vary significantly since the total oscillation flow rate is not changing. If we use electrical circuit to analyze the oscillation flow (Figure 3.5 (A)), this circuit is powered by a voltage source (oscillation pressure). When resistance in oscillation channels are much bigger than the oscillation resistance in sorting area, the constant voltage source and oscillation channels' resistance can be combined together to work as a constant current source (Figure 3.5 (B)). Specifically, the total flow rate in oscillation direction is constant. To obtain a design where the hydrodynamic resistance of the oscillation channels is dominant, oscillation channel width and height are selected based on aspect ratios that could be obtained via standard photolithographic microfabrication processes.

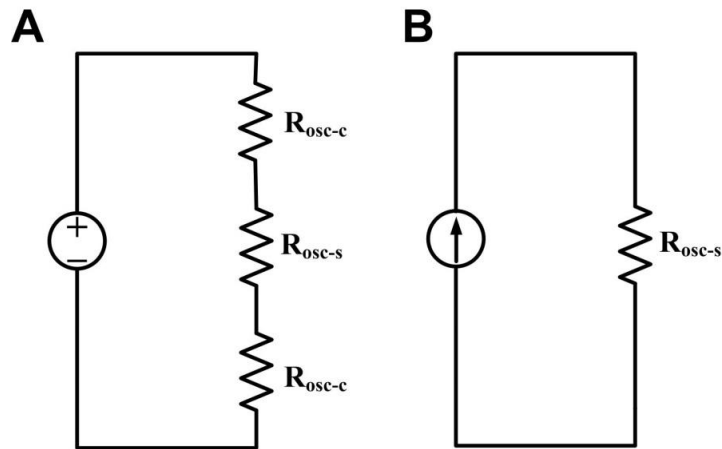


**Figure 3.5 Circuit analysis of the oscillation flow (A). The voltage source can equal to a current source when oscillation channels' resistance is dominant (B).**

For even distribution of oscillation flow in the ratchet matrix from the left edge to the right edge, there should be no significant buffer pressure drop from the left edge to the right edge. As a result, the buffer resistance of the sorting area should be much smaller than the total resistance of buffer channel and outlet channels:

$$R_{buffer-c} + R_{outlet} \gg R_{buffer-s} \quad (3.8)$$

Therefore, the total hydrodynamic resistance of the buffer channel and outlet channels is similarly designed to be dominant in the buffer direction.

### 3.3 Resistance of Funnel Matrix

As shown in Equation 3.5, we need to determine both total oscillation flow rate ( $Q_{Tosc}$ ) and one row cutoff funnels' total oscillation resistance ( $R_{cutoff}$ ) in order to determine the pressure difference of the cutoff funnels ( $\Delta P_{cutoff}$ ). The total oscillation flow rate ( $Q_{Tosc}$ ) is also related to the sorting area's oscillation resistance. In this section, we will calculate the oscillation resistance of the cutoff funnels and the sorting area's oscillation resistance.

The central separation area is composed of 32 rows by 512 columns for the 1× device and 32 rows by 2048 columns for the 4× extended device. The height of the sorting area should be big enough to allow cell to deform through the funnel but not to block pores, and also small enough to ensure fabrication accuracy. We assume that each element has an oscillation resistance  $r_i$  and a buffer resistance  $r_j$ . By using COMSOL, we can calculate both resistances. Then the total oscillation and buffer resistance of the sorting area can be derived by considering series and parallel connection of these resistance elements. Here we calculated 6  $\mu\text{m}$ -funnel gap's oscillation resistance and buffer resistance as an example. Other funnels are calculated by using the same method.

For the oscillation resistance  $r_i$ , we firstly drew two models of 9 funnel gaps and 8 funnel gaps paralleling in buffer direction in SolidWorks with a height of 30  $\mu\text{m}$  and imported it into COMSOL. We simulated these two funnel units in COMSOL with 10,000 Pa as applied pressure difference from the inlet to outlet (Figure 3.6). Figure 3.7 show the flow velocity between the funnels. The model with 9 funnel gaps has a total vertical flow rate of  $1.779 \times 10^{-9} \text{ m}^3/\text{s}$  while the one with 8 funnel gaps has a total vertical flow rate of  $1.581 \times 10^{-9} \text{ m}^3/\text{s}$ . So one 6  $\mu\text{m}$ -funnel gap's vertical flow rate is  $0.198 \times 10^{-9} \text{ m}^3/\text{s}$  and the oscillation resistance of one 6  $\mu\text{m}$ -funnel gap can be calculated as:

$$R_{osc-6} = \frac{P_{osc-6}}{Q_{osc-6}} = \frac{10000 \text{ Pa}}{0.198 \times 10^{-9} \text{ m}^3/\text{s}} = 5.051 \times 10^{13} \text{ Pa} \cdot \text{s}/\text{m}^3 \quad (3.9)$$

which is  $5.051 \times 10^{13} \text{ Pa} \cdot \text{s}/\text{m}^3$ .

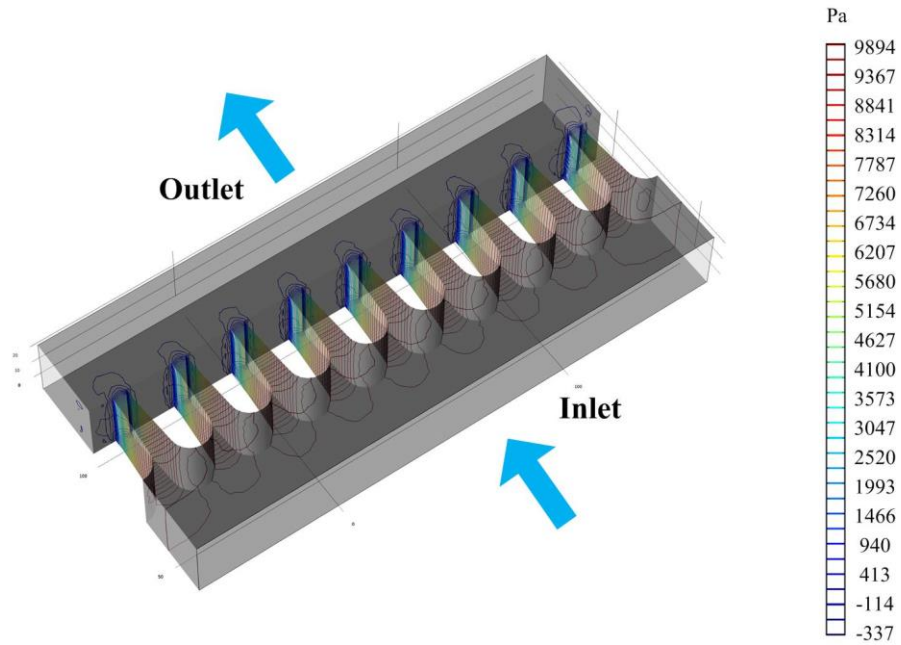


**Figure 3.6 Pressure drop in 6 μm-funnel gap when pressure is applied on the bottom face.**

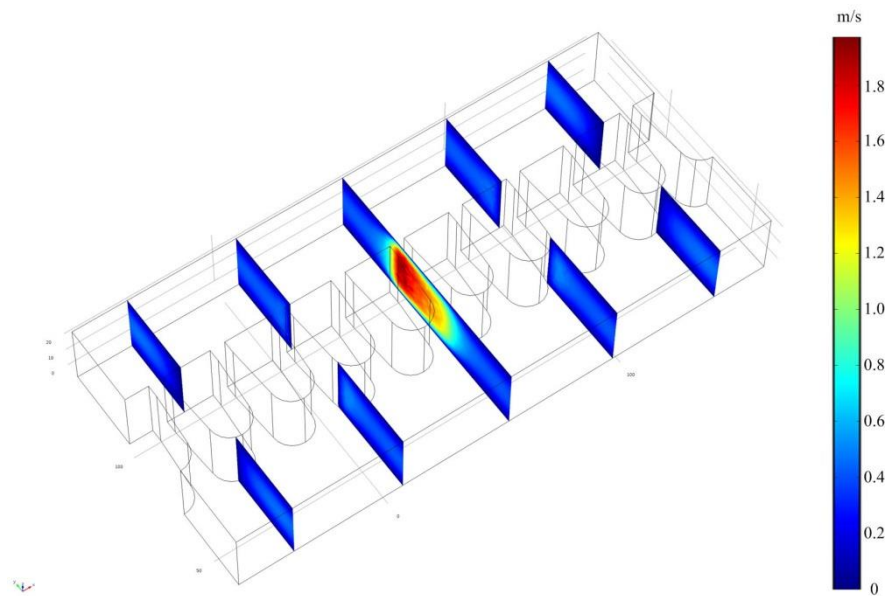


**Figure 3.7 Flow velocity in 6 μm-funnel gap.**

When calculating the buffer resistance of funnels, we parallel 10 funnel gaps and 9 funnel gaps in the oscillation direction and apply pressure in the buffer direction (Figure 3.8). Using the same method as before, we can get each element's buffer resistance  $r_j$ .

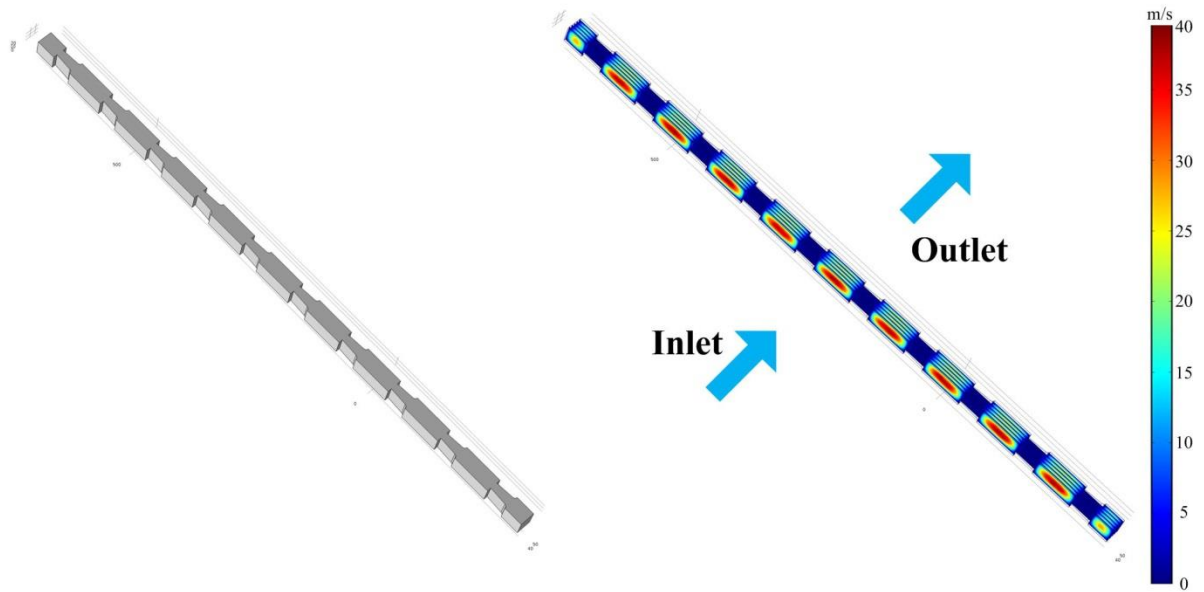


**Figure 3.8 Model of ten 12  $\mu\text{m}$ -funnel gaps in series and flow velocity simulation under 10,000 Pa pressure difference in horizontal direction.**

By considering the central sorting area as series and parallel connections of  $r_i$  and  $r_j$  respectively (Equation 3.1 and 3.2), we calculated the total oscillation and buffer resistance and cutoff funnels' oscillation resistance as shown in Table 3.1 in Section 3.4.

### 3.4 Resistance of Supporting Microchannels and Flow Rate

#### 3.4.1 Resistance of Supporting Microchannels

We used COMSOL 4.0 to simulate the flow in each component microchannel and calculate their resistance (Figure 3.1). Both the oscillation flow rate (Equation 3.3) and the buffer flow rate (Equation 3.4) can be calculated from the applied pressure and the hydrodynamic resistance determined by simulation. Here, we present the determination of the buffer inlet channel resistance as an example. First, we drew the model of the buffer channel in SolidWorks and imported it into COMSOL. Then the model is meshed with physics-controlled elements as shown in Figure 3.9 (A). When applying 10,000 Pa at the inlet face and 0 Pa at the outlet, we can see how the pressure drops along the channel and the flow velocity difference inside the channel (Figure 3.9 (B)). The volumetric flow rate ( $Q$ ) through the buffer inlet channel is  $1.044 \times 10^{-10} \text{ m}^3/\text{s}$ , so the total resistance of the buffer inlet channel can be calculated as:

$$R_{buffer-c} = \frac{P_{buffer-c}}{Q_{buffer-c}} = \frac{10000 Pa}{1.044 \times 10^{-10} m^3/s} = 9.615 \times 10^{13} Pa \cdot s/m^3 \quad (3.10)$$

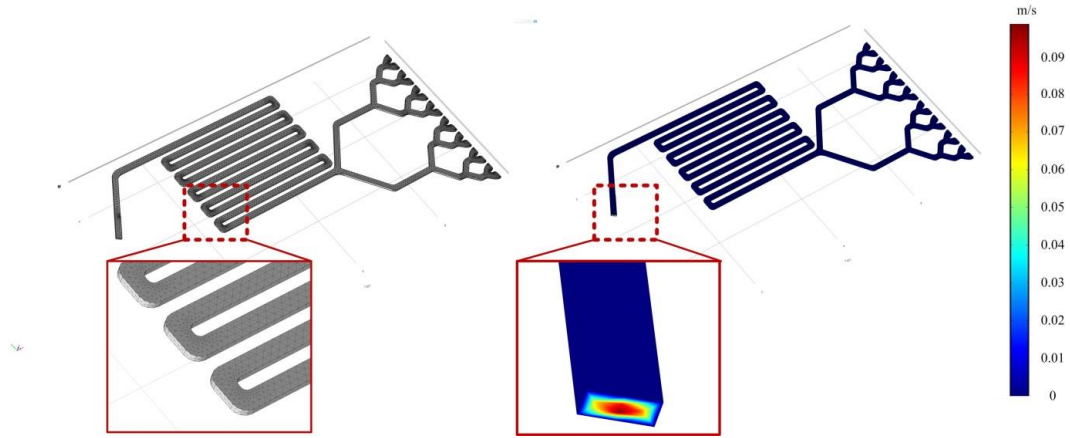


**Figure 3.9** Flow simulation of the buffer channel in COMSOL. (A) Physics-controlled mesh of buffer inlet channel. (B) Simulation of flow velocity inside the channel.

Using this method, we calculated other channels' resistances as well and presented in Table 3.1.

**Table 3.1** Device components and resistance.

Component	Resistance (32×512 device) (pa•s/m <sup>3</sup> )	Resistance (32×2048 device) (pa•s/m <sup>3</sup> )
<b>Buffer inlet channel (<math>R_{buffer-c}</math>)</b>	$9.615 \times 10^{13}$	$9.615 \times 10^{13}$
<b>Sample inlet channel (<math>R_{sample}</math>)</b>	$2.695 \times 10^{13}$	$2.695 \times 10^{13}$
<b>Oscillation channels (<math>R_{osc-c}</math>)</b>	$1.830 \times 10^{13}$	$9.259 \times 10^{12}$
<b>Outlet channels (<math>R_{outlet}</math>)</b>	$6.783 \times 10^{13}$	$6.783 \times 10^{13}$
<b>Sorting Matrix (buffer direction, <math>R_{buffer-s}</math>)</b>	$4,196 \times 10^{12}$	$1.678 \times 10^{13}$
<b>Sorting Matrix (oscillation direction, <math>R_{osc-s}</math>)</b>	$9.064 \times 10^{11}$	$2.266 \times 10^{11}$
<b>Cutoff Funnels (oscillation direction, <math>R_{cutoff}</math>)</b>	$9.876 \times 10^{10}$	$2.469 \times 10^{10}$

As we discussed in Section 3.2, the resistance of the oscillation channels should be the dominant resistance in the oscillation flow to ensure a stable pressure difference of cutoff funnels. In the 32×2048 device, the resistance of the oscillation channels takes over 97% of the total resistance. Therefore, the oscillation flow can be considered as an oscillation resistance of sorting matrix powered by a current source. In this case, the oscillation flow through the cutoff funnels is constant as well as the pressure difference. Additionally, the resistance of buffer channel and outlet channels also comprises of >90% of the total resistance in the buffer flow direction. Therefore, the pressure drop in the sorting matrix is small enough to allow even distribution of oscillation flow.

From the 32×512 device to the 32×2048 device, ratio of the sorting matrix's oscillation resistance to the oscillation channel's resistance is decreased by half. According to the Equation 3.7, the flow in the 4× extended device will be more stable and the flow force on cells will be more constant than the 1× version.

### 3.4.2 Flow Rate Calculation

As stated in Equation 3.3 and Equation 3.4, the flow rate in the oscillation direction and the buffer direction can be calculated by the total pressure difference and total resistance. Here we calculate the oscillation flow rate as an example.

If we apply 27,000 Pa at the oscillation inlet, we can calculate total oscillation flow rate at the cutoff funnel by using Equation 3.6 as:

$$Q_{Tosc} = \frac{P_{osc}}{2 \times R_{osc-c} + R_{osc-s}} = \frac{27,000}{2 \times 9.259 \times 10^{12} + 2.266 \times 10^{11}} \quad (3.11)$$

$$= 1.44 \times 10^{-9} m^3/s$$

So the volumetric flow rate in each funnel is:

$$Q_{funnel} = \frac{Q_{Tosc}}{Funnel\ number} = \frac{1.44 \times 10^{-9}}{2048} = 7.03 \times 10^{-13} m^3/s \quad (3.12)$$

We can also calculate in the total volume of buffer that flows in one hour from the forward pressure inlet to the backward pressure inlet. In one oscillation cycle, the forward flow lasts 3 seconds and the backward flow lasts 1 second:

$$\begin{aligned}
 V &= Q_{Tosc} \times 3600s \div 4 \times (3 - 1) = 1.44 \times 10^{-9} \times 3600 \div 4 \times 2 & (3.13) \\
 &= 2.59 \times 10^{-6} m^3
 \end{aligned}$$

which corresponds to 2.59 ml of buffer per hour. This result has been confirmed by experiments.

### 3.5 Reliable Cell Sorting

#### 3.5.1 Variation in Oscillation Resistance of Cutoff Funnels

As shown in Equation 3.5, the pressure difference of the cutoff funnels is determined by the total oscillation flow rate and the resistance of the cutoff funnels. When cells are captured in the cutoff funnels, the oscillation resistance of the cutoff funnels is modified which may lead to a variation in the pressure difference of the cutoff funnels. Here, we analyze the variation in the oscillation resistance of the cutoff funnel row when some of the funnels are occupied by cells.

First, we need to calculate the variation in single funnel resistance when the funnel is occupied by one cell. A cell model is added onto the model with 9 funnels in Section 3.3. We simulated this model with the cell located at the bottom of one of the funnels (Figure 3.10) and captured in a funnel (Figure 3.11) with 10,000 Pa pressure difference applied in the oscillation direction. There is no flow rate change between the model without cell (Figure 3.7) and the model with a cell at the bottom (Figure 3.10). However, the flow rate changes from  $1.779 \times 10^{-9} \text{ m}^3/\text{s}$  to  $1.699 \times 10^{-9} \text{ m}^3/\text{s}$  when a cell is captured at a funnel. The corresponding resistances of the funnel will change from  $5.051 \times 10^{13} \text{ Pa}\cdot\text{s}/\text{m}^3$  to  $8.475 \times 10^{13} \text{ Pa}\cdot\text{s}/\text{m}^3$ . The resistance of a single funnel is then increased by 67.6%.

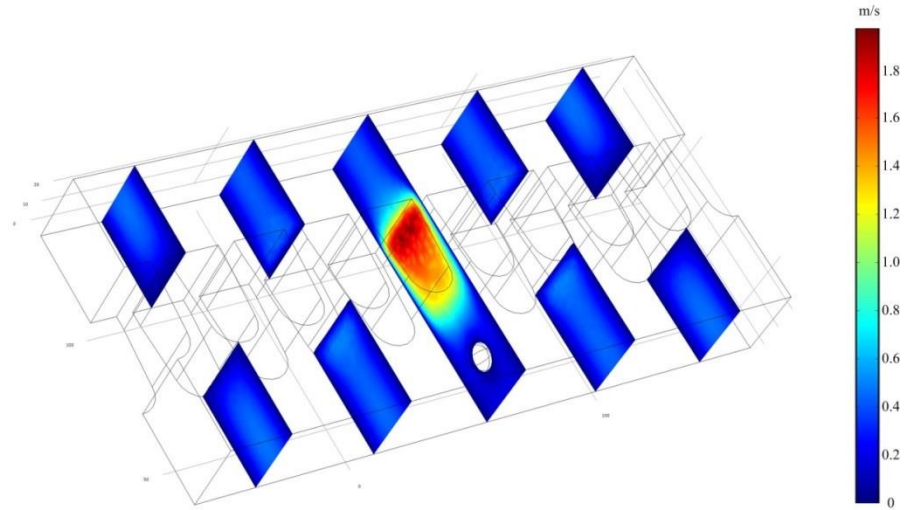


**Figure 3.10 Flow velocity simulation of 6  $\mu\text{m}$ -funnel gaps with a cell at the bottom.**

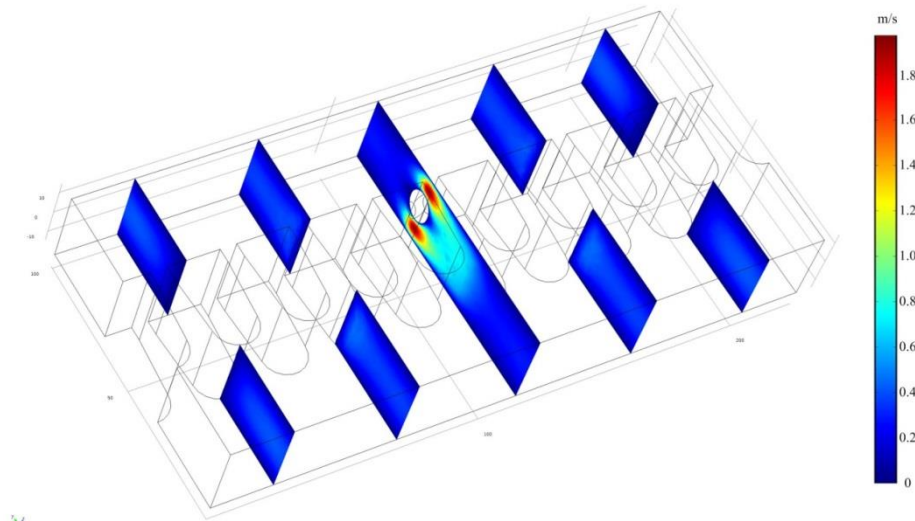


**Figure 3.11 Flow velocity simulation of 6  $\mu\text{m}$ -funnel gaps with a cell in a funnel.**

The variation of the cutoff resistance is related to the number of funnels occupied by cells. As CTCs are very rare in the blood, we neglect the number of funnels occupied by them. The number of leukocytes captured in cutoff funnels at the same time is related to the throughput of the device which is the number of leukocytes that can be processed per hour. To calculate the number of cutoff funnels that are occupied by leukocytes, we made the following assumptions: 1. the retention of leukocytes in the CTC outlet is 0.1%; 2. it takes 5 oscillation cycles for the leukocytes to travel from the beginning to the end of the sorting area and each oscillation cycle lasts 4 seconds; and 3. these retention portion of leukocytes are all captured in the cutoff funnels. Then we can calculate the number of the cutoff

funnels occupied by leukocytes ( $N_{occupied}$ ) when the forward pressure is applied as follow:

$$\begin{aligned} N_{occupied} &= throughput \times retention\ ratio \times time \\ &= (throughput \div 3600) \times 0.1\% \times (4 \times 5) \end{aligned} \quad (3.14)$$

Then the number of vacant funnels can be expressed as:

$$N_{empty} = 2048 - N_{occupied} \quad (3.15)$$

Then the resistance of the cutoff funnels in the oscillation direction is paralleling  $N_{occupied}$  funnels with cells ( $R_{cell}$ ) and  $N_{empty}$  empty funnels ( $R_{empty}$ ):

$$R'_{cutoff} = \frac{1}{\frac{N_{occupied}}{R_{cell}} + \frac{N_{empty}}{R_{empty}}} = \frac{1}{\frac{N_{occupied}}{8.475 \times 10^{13}} + \frac{N_{empty}}{5.051 \times 10^{13}}} \quad (3.16)$$

The resistance of a row with all empty cutoff funnels is:

$$R_{cutoff} = \frac{R_{empty}}{2048} = \frac{5.051 \times 10^{13}}{2048} = 2.469 \times 10^{10} \text{ pa} \cdot \text{s/m}^3 \quad (3.17)$$

So the variation in the resistance can be derived by Equation 3.14~Equation 3.17:

$$Variation = \left| \frac{R'_{cutoff}}{R_{cutoff}} - 1 \right| = \frac{throughput \times 0.7072 \times 10^{-9}}{1 - throughput \times 0.7072 \times 10^{-9}} \quad (3.18)$$

The relationship between the oscillation resistance of cutoff funnels and throughput is shown in Figure 3.12.

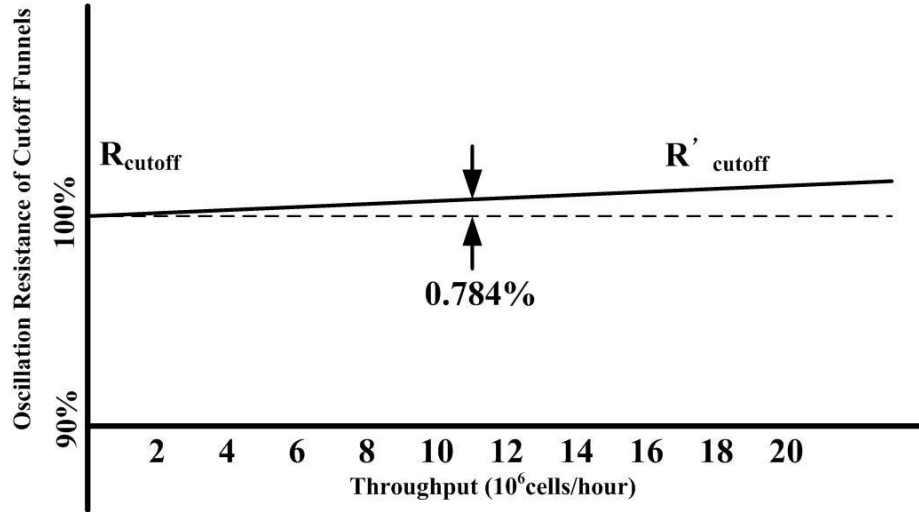


**Figure 3.12 The relationship between the oscillation resistance of cutoff funnels and throughput.**

To estimate the theoretical throughput of the device, we took leukocytes' vertical velocity as  $1 \times 10^{-4}$  m/s (analyzed from video). For each funnel, 4 cells can go through in 1 second. If we assume that half of the cutoff funnels can be simultaneously used for cell sorting, then 256 funnels can be used for the  $1 \times$  device, while 1024 funnels gaps can be used for the  $4 \times$  extended device. An oscillation cycle has a duration of 4 seconds, of which 3 seconds is for the forward pressure and 1 second for the backward pressure. Then 2700 seconds per hour is used for sorting. So the estimated the throughput for  $1 \times$  device is:

$$\text{Throughput}_{1 \times \text{ device}} = 4 \times 2700 \times 256 = 2.8 \times 10^6 \text{ cells/hour} \quad (3.19)$$

So the throughput is  $2.8 \times 10^6$  leukocytes per hour for the  $1 \times$  device and  $11.1 \times 10^6$  leukocytes per hour for the  $4 \times$  extended device.

If we infuse  $11 \times 10^6$  leukocytes per hour for the throughput in Equation 3.18, we can calculate that the variation in the resistance is only 0.784% (Figure 3.12). Variation is small enough to be neglected. As the experimental throughput is less than the theoretical throughput, the variation will be even smaller.

### 3.5.2 Variation in Total Oscillation Flow Rate

As stated in the last section, the variation in resistance of the cutoff funnels can be neglected when cells are captured in the cutoff funnels. Another key factor in determining pressure difference of cutoff funnels is total oscillation flow rate. Here we will analyze how  $Q_{Tosc}$  is modified by cells captured in the ratchet matrix.

When the sample is being processed, some funnels at the top right region of the ratchet matrix are occupied by leukocytes and the resistance of the whole filter consequently increases. To estimate the total oscillation resistance variation of the sorting area, we separate the sorting area into resistance units, as shown in Figure 3.13. When there is no cell captured in the funnel matrix, the resistance distribution in the sorting area can be expressed as Figure 3.13 (A). When cells are loaded into sorting area for separation, the top right region's resistance is increased. Here we consider the worst case where all funnels at the top right are occupied by leukocytes. So each funnel resistance is increased by 67.6% which results in resistance increase in the top right region (Figure 3.13 (B)).

We then use COMSOL to simulate the resistance units in Figure 3.13 and calculate the variation in the resistance of whole sorting area. From the case in Figure 3.13 (A) to the case in Figure 3.13 (B), the oscillation resistance of the whole sorting area is increased by 8.1%.

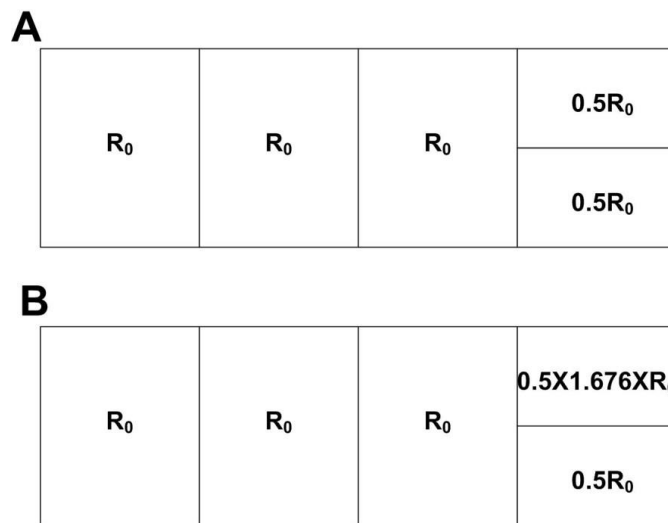


**Figure 3.13 Schematic analysis of the filter resistance when no cell is captured (A) and when all the funnels at the top right are occupied by cells (B).**

If we use Equation 3.6 and Table 3.1 to calculate the flow rate, we see that when there is no cell captured in the funnel matrix:

$$Q_{Tosc} = \frac{P_{osc}}{2 \times R_{osc-c} + R_{osc-s}} \quad (3.20)$$

$$= \frac{P_{osc}}{2 \times 9.259 \times 10^{12} + 2.266 \times 10^{11}} \text{ m}^3/\text{s}$$

When all the funnels at the top right are occupied by cells:

$$Q'_{Tosc} = \frac{P_{osc}}{2 \times R_{osc-c} + R_{osc-s}} \quad (3.21)$$

$$= \frac{P_{osc}}{2 \times 9.259 \times 10^{12} + 1.081 \times 2.266 \times 10^{11}} \text{ m}^3/\text{s}$$

So the change of flow rate during the forward pressure is:

$$\frac{Q'_{Tosc}}{Q_{Tosc}} = 0.999022 \quad (3.22)$$

which is only a 0.0978% variation.

The variation in the resistance of cutoff funnels and variation in total oscillation flow rate are both small enough to be neglected. Therefore, the pressure difference of cutoff funnels can be kept stable when the number of cells captured in the funnel matrix and the cutoff funnels are changing.

### 3.6 Summary

This chapter described the design of a continuous cell separation device based on the microfluidic ratchet mechanism. The device is composed of a central sorting area and other microchannels for flow control (Figure 3.14). The key factor in design is to ensure that the pressure difference of cutoff funnels is stable. To achieve this goal, the column number of funnels is enlarged to 2048 to ensure that the resistance of cutoff funnels will not change when cells are captured in the cutoff funnels. At the same time, the resistance of oscillation channels is designed to be the dominant resistance in the oscillation flow so that variation in the oscillation resistance of sorting area will not

affect the total flow rate in the oscillation direction.

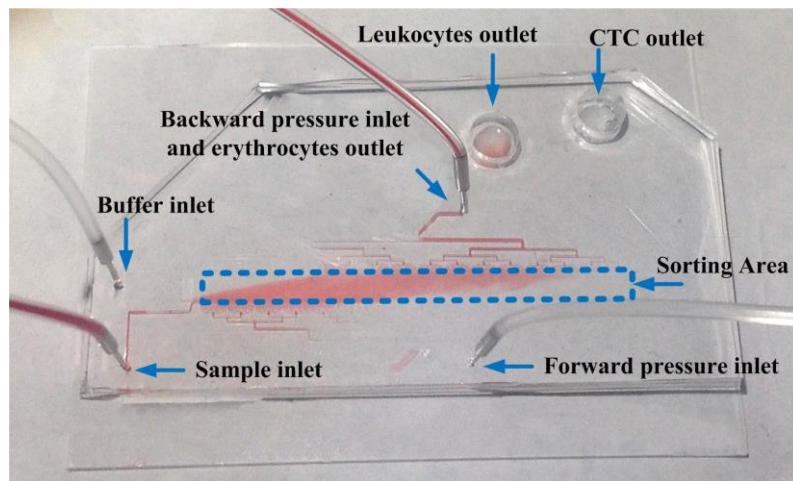


**Figure 3.14** A continuous cell separation device based on the microfluidic ratchet mechanism.

## **Chapter 4: Fabrication and Experimental Procedures**

This chapter describes fabrication process and experimental procedure. The device is fabricated using standard techniques of photolithography and soft lithography. The desired pattern is first formed on a silicon wafer which is used as a master for replication in polydimethylsiloxane (PDMS) silicone. Then the PDMS device is treated with plasma and bonded to a glass slide. Detailed fabrication process is described in Section 4.1 and Section 4.2. Section 4.3 introduces sample preparation, followed by experimental setup and preparation in Section 4.4.

### **4.1 Fabrication of Silicon Masters**

Patterns for the microstructures are drawn using DraftSight (Dassault Systems, Vélizy-Villacoublay, France) and translated onto two commercially printed optical photomasks, one for the microscale constrictions, which requires higher resolution, and another one for the flow channels. Inverse master of the device is fabricated on silicon wafers using standard photolithography techniques. The microstructures are fabricated on a silicon wafer with two photolithographic layers. In the first layer, the silicon wafer is coated with epoxy-based negative photoresist SU-8 8025 (Microchem, Newton, MA) and spun at a speed of 3000 rpm for 30 seconds. This layer is for central sorting constrictions and designed height for this layer is 30  $\mu\text{m}$ . The wafer is baked on a 95 °C hotplate for 5 minutes followed by UV exposure through the optical photomask (Advance Reproductions, Andover, MA). The wafer is then baked at 65°C, 95 °C and 65 °C for 1, 4 and 1 minute respectively. The patterned wafer is developed using SU-8 developer (Microchem, Newton, MA) and washed with isopropanol. A second photomask (CAD/Art Services, Brandon, OR) with flow channel features are aligned to the first pattern with align markers and a second set of SU-8 features are patterned and developed following the same procedures except for adjusting spin speed to 2200 rpm for 30 seconds. The designed height for this layer is 40 $\mu\text{m}$ . To harden the patterned SU-8 microstructures, the wafer is paced on a hot plate and the temperature is ramped from 40 °C at 15 °C every 10 minutes until 165 °C is reached. After the wafer is baked for 30 minutes at 65 °C, the

hotplate temperature is ramped down at a rate of 50 °C every 10 minutes. The wafer is removed when the hotplate temperature reaches 65 °C. The measured height of the first layer is 29.6 μm and the second layer is 40.1 μm. Fabrication process of silicon masters is shown in Figure 4.1.

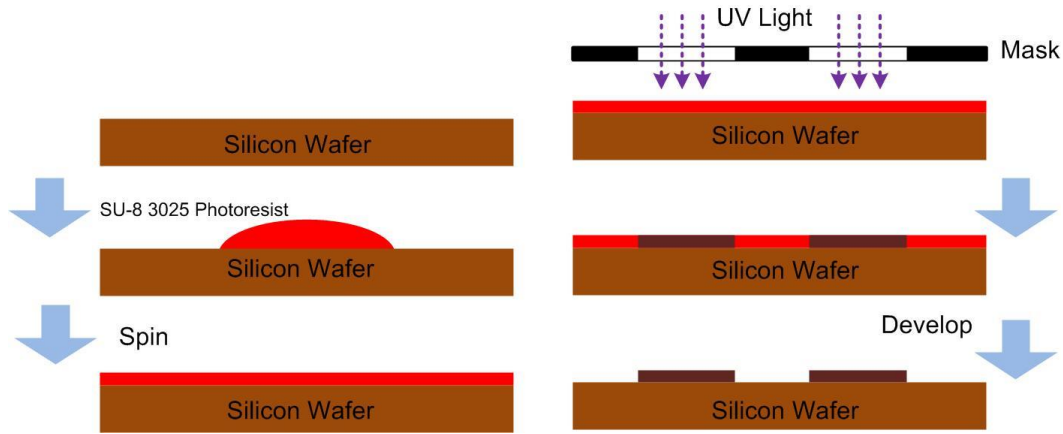


**Figure 4.1 Fabrication process of silicon masters.**

## 4.2 Fabrication of PDMS Devices

The fabrication process of PDMS devices is shown in Figure 4.2.

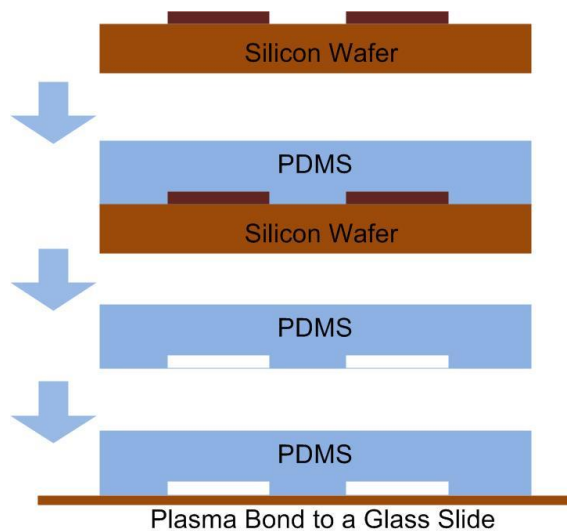


**Figure 4.2 Fabrication process of PDMS devices**

The Polydimethylsiloxane (PDMS) device is formed using 10:1 base to hardener ratio of Sylgard 184 silicon (Dow Corning, Midland, MI) on the wafers with reverse features. The mixed PDMS is

vacuumed for 15 minutes to get rid of air bubbles in the features. After being baked for 2 hours, the PDMS device is then peeled off gently from the master wafer; inlets and outlets are punched manually using 0.5 and 6 mm punches (Harris, Redding, CA). The PDMS device is subsequently bonded to a glass slide following 90 seconds activation in air plasma (Harrick Plasma, Ithaca, NY).

### **4.3 Sample Preparation**

Device characterization experiments were conducted using whole blood and a highly invasive EpCAM-negative cell line, UM-UC13 (UC13) bladder cancer cells. Whole blood was drawn from healthy donors into 6 ml EDTA blood collection tubes. Hoechst (Invitrogen, Burlington, ON) was added into whole blood for staining leukocytes. The UC13 cells were kindly provided by Pathology Core of the Bladder Cancer SPORE at MD Anderson Cancer Center. They were cultured in MEM solution with the addition of 10% (v/v) fetal bovine serum, 1% L-glutamine, 1% MEM Non-Essential Amino Acids, 1% Sodium Pyruvate (Invitrogen, Burlington, ON), and 1% Penicillin Streptomycin (Fisher Thermo Scientific, Waltham, MA), and incubated at 37°C in a humidified environment with 5% CO<sub>2</sub>. Cancer cells were used for experimentation 3 days after passaging. Before doped into whole blood, cancer cells were stained with Calcein AM (Invitrogen, Burlington, ON) and washed with Phosphate Buffered Saline (PBS).

In the experiments that assess cell viability, UC13 cells were fluorescently stained with a live/dead assay (CalceinAM and ethidium homodimer) before doped into whole blood. Viability of UC13 is checked before and after running the device. Viability of sample is defined as the number of live cells over the total number of cells (live and dead cells).

### **4.4 Experimental Setup and Procedure**

Fluid controlling actuators employed in experiments include a commercial pressure controller (Fluigent, Paris, France), and the custom made pressure board (Figure 4.3) designed by Hongshen Ma. Pressure board control software is kindly designed by Richard Ang. Experiments were conducted under an inverted microscope (TS-100, Nikon, Tokyo, Japan), and a CCD camera (DS-2MBW, Nikon, Tokyo, Japan).

The initial count for the number of UC13 and leukocytes in whole blood is determined manually using a hemacytometer. A microscope with encoded stage is used to take fluorescence images of the collection reservoir with a 4× objective. The resulting images are stitched together using Microsoft Image Composite Editor. The number of target and contaminant cells is then counted manually from the composite images. The performance metrics of yield, depletion ratio and enrichment is calculated from the count values.



**Figure 4.3 The pressure board. (1) Forward pressure regulators. (2) Backward pressure regulators. (3) Forward pressure manifolds along with solenoid valves. (4) Backward pressure manifolds along with solenoid valves. (5) Microcontroller and circuit board system.**

For each experiment, the PDMS microfluidic devices were firstly filled with PBS with 0.2% Pluronic, then incubated for 15 minutes to prevent non-specific adsorption of cells at the walls. Then whole blood doped with UC13 cells is loaded from the sample inlet, at the same time, the oscillation pressure is turned on for cell sorting. For system characterization on oscillation pressure, different pressure is applied to the oscillation inlets. Characterization on doping ratio is conducted with samples of different leukocytes to UC13 ratios. The oscillation pressure in these experiments was the same. After separation, the device was put aside for 1 hour to let cells settle down to the bottom of the reservoir before fluorescence images of the collection reservoir were taken.

## **Chapter 5: System Characterization and Discussion**

Performance metrics of the CTC separation device include the yield of cancer cells, depletion ratio of leukocyte, and enrichment of the cancer-cell-to-leukocyte ratio. Section 5.1 describes the system characterization method. Section 5.2 describes the measurement of the size of leukocytes and of cultured cancer cells. Section 5.3, 5.4 and 5.5 describe pressure optimization, doping ratio optimization and viability of the device respectively. Section 5.6 describes the performance comparison between size based separation methods and ratchet mechanism based separation. Section 5.7 concludes the chapter with a discussion on separation results on blood samples doped with cultured cancer cells.

### **5.1 System Characterization**

To evaluate the performance of the microfluidic ratchet device, UM-UC13 human bladder cancer cells were doped into whole blood from healthy donors at the ratio of 1:1000. UC13 cancer cells were stained with Calcein AM while leukocytes were stained with Hoechst to be observed under fluorescent microscope. Before samples were loaded, the device was incubated with PBS and 0.2% Pluronic to prevent non-specific adsorption of cells at the walls. By observing cell distribution in the sorting area while a sample is processed, we can optimize the system performance by varying the applied pressure in the oscillation, sample inlet, and buffer inlet channels (Figure 5.1). With greater oscillation pressure, more cells will distribute above the cutoff funnel row. Correspondingly, with smaller oscillation pressure, more cells will remain below the cutoff funnel row. The system performance is assessed using cancer cell yield, depletion ratio of leukocytes, and enrichment of the cancer-cell-to-leukocyte ratio. Purity can vary considerably depending on the concentration of CTCs in the patient's blood or the construction of the model samples (e.g. sample doping ratio). Therefore, purity is not used for system characterization but will be reported for post-separation analysis.

After each experiment, the device was stored in darkness for 1 hour to allow the cells to settle to the surface of the glass slide substrate. Then, fluorescent images were taken of both the cancer cell

and leukocytes outlet wells (Figure 5.2). Cancer cell numbers in cancer cell outlet and leukocyte outlet were counted manually to calculate yield. Leukocyte number in cancer cell outlet was counted manually to calculate depletion ratio and enrichment.

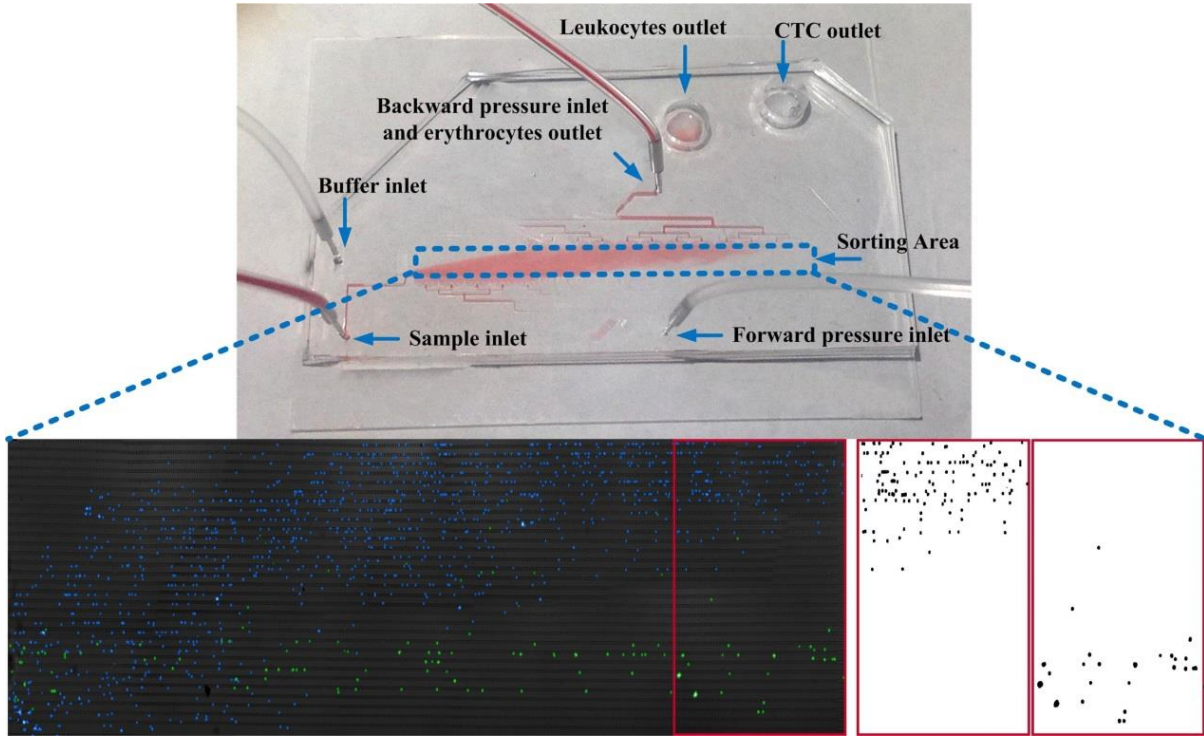


**Figure 5.1** Micrograph of cell distribution in sorting region: Leukocytes are stained with Hoechst (blue) and UC13 are stained with Calcein AM (green).

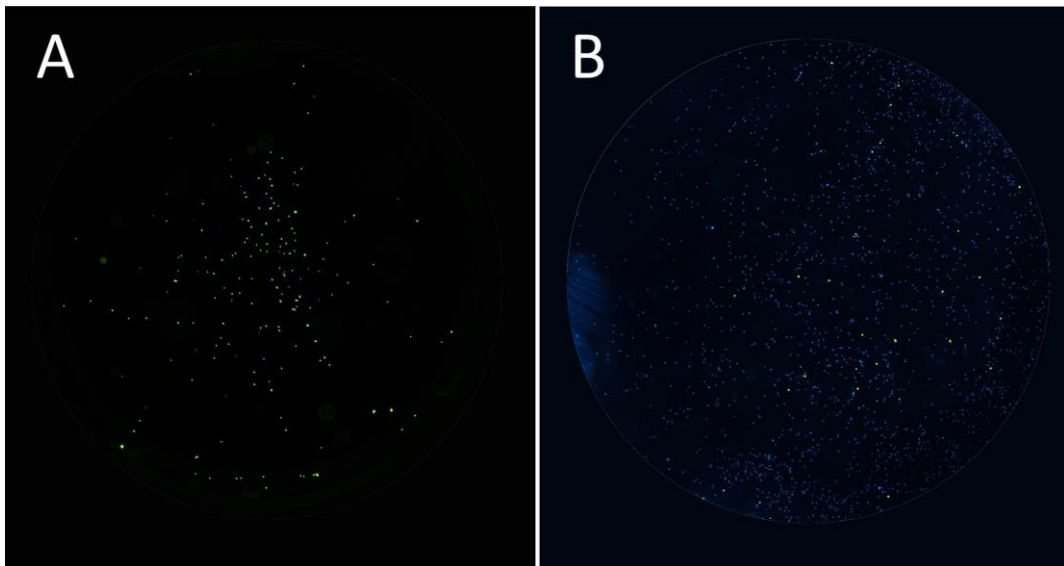


**Figure 5.2** Fluorescent image of the CTC outlet well (A) and leukocyte outlet well (B). UM-UC13 cells were stained with Calcein AM (green) and leukocytes were stained with Hoechst (Blue).

## 5.2 Cell Diameter

We measured the diameter of 100 UM-UC13 cultured cancer cells and leukocytes from a healthy volunteer in suspension in PBS. Measurement was conducted under an inverted microscope (TS-100, Nikon, Tokyo, Japan), and a CCD camera (DS-2MBW, Nikon, Tokyo, Japan). Both cultured cancer cell and leukocytes exhibit a spherical shape when suspended. The mean diameter of leukocytes was found to be  $9.92 \pm 1.80 \mu\text{m}$ , while the mean diameter of UM-UC13 was  $17.60 \pm 2.90 \mu\text{m}$ . The size distribution of both cell types is shown in Figure 5.3. It's important to note that cultured cancer cells cannot exactly represent CTCs, as CTCs are typically smaller in size<sup>23</sup>. However, cultured cancer cells nonetheless represent a useful model to characterize our system because of their simple availability and relative consistency.

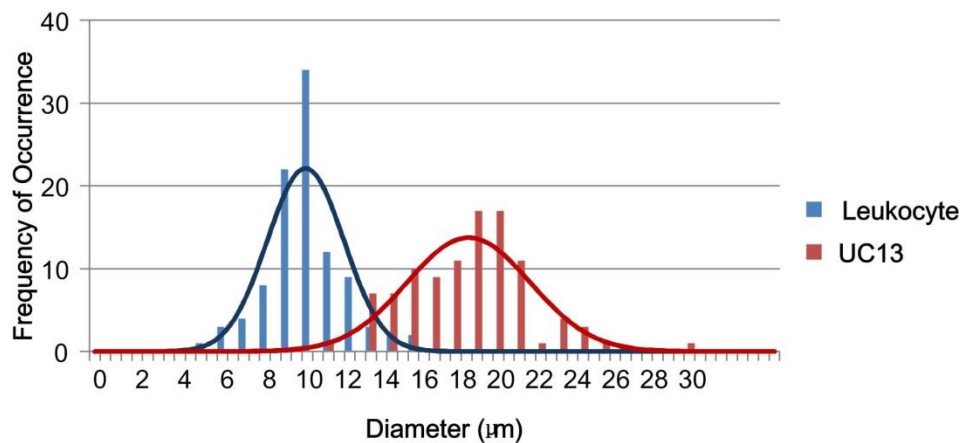


**Figure 5.3 Size distributions of leukocytes (blue) and UC13 (red).**

## 5.3 Pressure Optimization

We varied the oscillation pressure to see how the applied pressure difference would influence yield, leukocyte depletion, and cancer cell enrichment. As discussed in Chapter 3, the pressure difference across the cutoff funnels can be determined from the total oscillation flow rate and the resistance of cutoff funnels. The total oscillation flow rate is derived from the oscillation pressure and the total oscillation resistance. Therefore, the pressure difference across the cutoff funnels derives from the oscillation pressure.

We optimized the system performance and oscillation pressure by observing cell distribution in

the sorting area as the cell sample is being sorted. With greater oscillation pressure, more cells will distribute above the cutoff funnels because of the higher pressure difference. However, more cells will stay below the cutoff funnels when a smaller oscillation pressure is applied. In experiments, we observed that when oscillation pressure is varied from 24,800 Pa to 35,300 Pa, leukocytes and CTCs achieved characteristic distributions ranging from the top and bottom of the funnel array respectively. This oscillation pressure range corresponds to a pressure difference across the cutoff funnels to range from 32.70 Pa to 46.32 Pa respectively. We chose four oscillation pressure settings from 24,800 Pa to 35,300 Pa. For each oscillation pressure setting, four repeated experiments were conducted to obtain the average and the range of yield, depletion ratio of leukocytes and enrichment. Considering the cancer cell capture yield, we observed that increased pressure difference corresponded to a reduced efficiency in cancer cell yield, from 90% at 32.70 Pa to 77% at 46.32 Pa (Table 5.1 and Figure 5.4 (A)). Specifically, when the pressure difference increases, greater forces are applied to the cells causing them to transit through the cutoff. As a result, a fraction of the smaller and more deformable UM-UC13 cells pass the cutoff row, leading to a decrease in yield. Simultaneously, however, a larger fraction of leukocytes are pushed past the cutoff funnel row, which reduces leukocyte contamination in the UM-UC13 outlet. The depletion ratio of leukocytes is positively related to volumetric flow rate as shown in (Table 5.2). Since the percentage of leukocytes eliminated from the UM-UC13 outlet is greater than the percentage of UM-UC13 cells that are lost, the enrichment is increased as the pressure difference of cutoff funnels increases. For example, an increase in applied pressure difference from 32.70 Pa to 46.32 Pa resulted in a 2.6-fold increase in enrichment of the cancer cells (Table 5.3 and Figure 5.4 (B)). At smaller pressure difference, the forces acting on the cells are gentler and cells are retained by larger pores leading to an increase in yield, but also results in greater leukocyte contamination which reduces enrichment. Therefore, we resolved to operate the device at a lower pressure to maximize the capture of potentially rare cells, for the purpose of cancer cell enumeration. However, we can achieve greater sample purity for CTC characterization by operating the device at higher applied pressure, at the expense of capture efficiency. In summary, we can optimize either yield or enrichment of the cancer cells in the separated sample by varying the

magnitude of the pressure difference. These results on both ends of the high yield and high enrichment spectrum are competitive with current technologies<sup>62,64,98,99</sup>.

**Table 5.1 Relationship of pressure difference of cutoff funnels and the yield of cancer cells.**

Oscillation pressure	Pressure difference of cutoff funnels	Yield of cancer cells	Error	
24,800 Pa	32.70 Pa	90.18%	+2.48%	-4.03%
28,300 Pa	37.24 Pa	81.42%	+3.47%	-4.73%
31,800 Pa	41.78 Pa	79.95%	+2.59%	-6.48%
35,300 Pa	46.32 Pa	76.56%	+3.81%	-5.92%

**Table 5.2 Relationship of pressure difference of cutoff funnels and the depletion ratio of leukocytes.**

Oscillation pressure	Pressure difference of cutoff funnels	Depletion ratio of leukocytes	Error	
24,800 Pa	32.70 Pa	99.9810%	+0.0081%	-0.0085%
28,300 Pa	37.24 Pa	99.9895%	+0.0019%	-0.0035%
31,800 Pa	41.78 Pa	99.9915%	+0.0035%	-0.0048%
35,300 Pa	46.32 Pa	99.9933%	+0.0035%	-0.0042%

**Table 5.3 Relationship of pressure difference of cutoff funnels and the enrichment.**

Oscillation pressure	Pressure difference of cutoff funnels	Enrichment	Error	
24,800 Pa	32.70 Pa	5,380	+2,801	-2,022
28,300 Pa	37.24 Pa	8,010	+926	-2,068
31,800 Pa	41.78 Pa	10,867	+5,557	-4,677
35,300 Pa	46.32 Pa	13,760	+9,946	-6,485

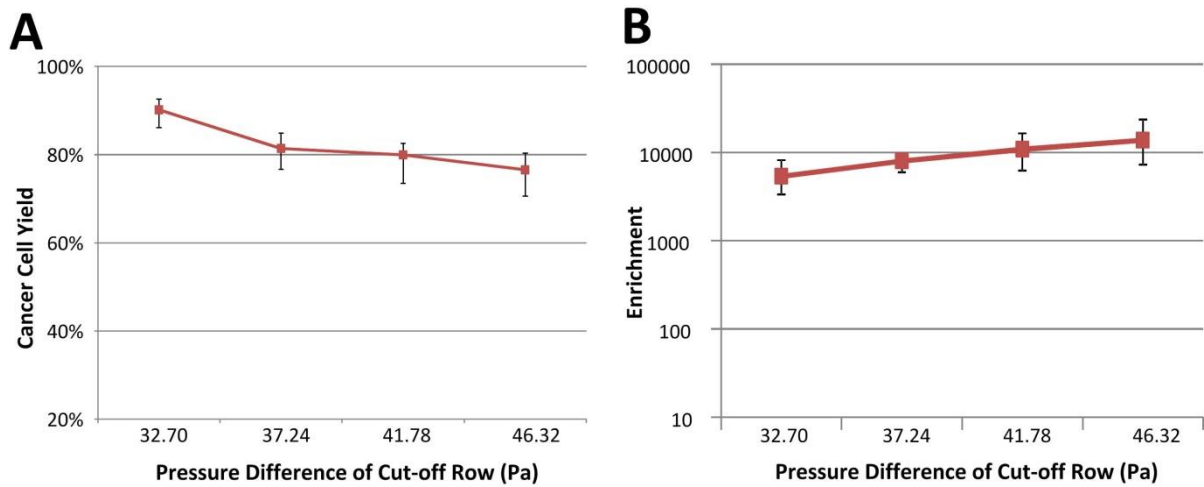


**Figure 5.4 Relationship of pressure difference of cutoff funnels and the yield of cancer cell (A), and enrichment (B).**

#### 5.4 Performance Dependence on Doping Ratio

While we observed that cancer cells could be effectively captured from contaminating leukocytes at a 1:1000 doping ratio, this ratio does not represent the extreme rarity of CTCs in patient blood. To evaluate the relationship between doping ratio and device performance, we assessed the enrichment and capture efficiency of cancer cells that are doped into leukocytes at different ratios. There was no observable alteration in cancer cell capture efficiency when they were doped into leukocytes at different cell density (Table 5.4 and Figure 5.5 (A)). The mean capture efficiency, irrespective of doping density was  $94.4 \pm 1\%$ . Interestingly, we observed that cancer cells were enriched at a greater rate when fewer cells were doped into leukocytes (Table 5.5 and Figure 5.5 (B)). When doping ratio is above 1:1000, the number of cutoff funnels occupied by UM-UC13 cannot be neglected. A decrease in the number of available cutoff funnels leads to insufficient depletion of leukocytes. For running patient blood, devices are working in high enrichment section with extreme rarity of CTCs.

**Table 5.4 Relationship of doping ratio and system performance.**

<b># of cancer cell spiked</b>	<b># of leukocytes loaded</b>	<b># of cancer cell recovered</b>	<b># of leukocytes retained</b>
34	820,000	32	111
79	820,000	73	181
237	820,000	225	125
474	820,000	454	183
610	820,000	571	149
1,356	820,000	1,284	224
3,446	820,000	2,375	491

**Table 5.5 Yield of cancer cells and enrichment calculated from Tabel 5.4.**

<b>Doping ratio of leukocytes to cancer cells</b>	<b>Yield of cancer cells</b>	<b>Enrichment</b>
24118	94.12%	8496
10380	92.50%	5121
3460	95.00%	7586
1730	95.83%	5236
1344	93.53%	6264
605	94.75%	4231
238	95.07%	1935

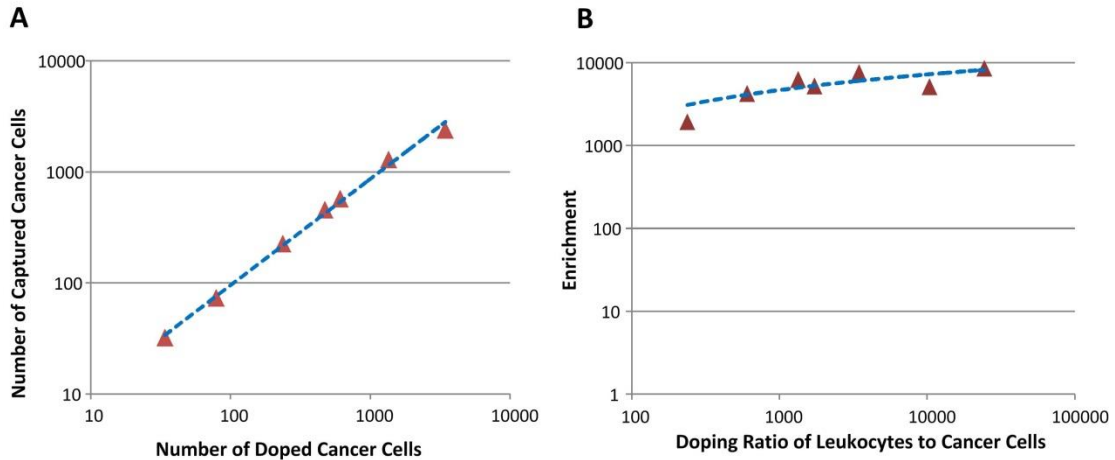


**Figure 5.5 Relationship of doping ratio and system performance. (A) Number of cancer cell captured and its relationship with number cancer cell doped. (B) Erichment and its relationship with doping ratio of leukocytes to cancer cells.**

## 5.5 Cell Viability

Cell viability after device was tested with live/dead kit. We first counted 535 cells from the prepared sample. There were 523 live cells and 12 dead cells. So the viability of the sample before running is 97.757%. Then we did 8 random experiments and counted the number of live cells and dead cells at the outlet of the device (Table 5.6). There were 2339 live cells and 75 dead cells in total from these 8 experiments. The viability of cells after running is 96.893% (+1.857%, -1.838%). So the viability of our system is 99.116% (+1.900%, -1.880%) calculated by Equation 1.5.

**Table 5.6 Numbers of live cells and dead cells at the cancer outlet of the device in 8 random experiments.**

# of live cells at outlet	# of dead cells at outlet	Viability
158	2	98.750%
169	4	97.688%
142	4	97.260%
199	9	95.673%
545	14	97.496%
377	13	96.667%
403	11	97.343%

# of live cells at outlet	# of dead cells at outlet	Viability
346	18	95.055%

Cells captured from outlet were further transferred into flask and cultured with MEM solution with the addition of 10% (v/v) fetal bovine serum, 1% L-glutamine, 1% MEM Non-Essential Amino Acids, 1% Sodium Pyruvate (Invitrogen), and 1% Penicillin Steptomycin (Fisher Thermo Scientific, Waltham, MA), and incubated at 37°C in a humidified environment with 5% CO<sub>2</sub>. By observing under a microscope, we can see that cells still keep high proliferation capability after 10 days (Figure 5.6).

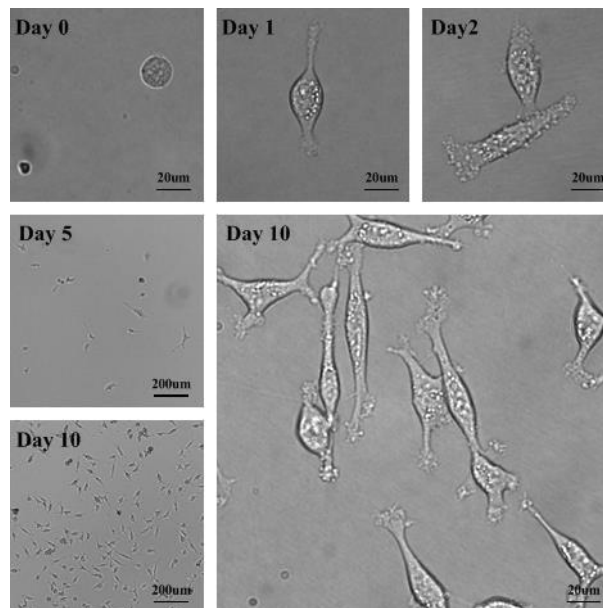


**Figure 5.6 Culture of cancer cells captured from device.**

## 5.6 Size and Deformability based Separation versus Size-only Separation

The microfluidic ratchet mechanism based device separates cells using a combination of size and deformability. Here we assess the improved ability to enrich for CTCs using our system versus size-only separation. As we measured the sizes of leukocytes and UM-UC13 cells in Section 5.2, the leukocytes had a mean diameter of  $9.92 \pm 1.80 \mu\text{m}$ , while UM-UC13 cancer cells had a mean diameter of  $17.60 \pm 2.90 \mu\text{m}$ . If the cell size conforms to a normal distribution and we imagine that each cell represents an immutable sphere, the cells would be displaced in the sorting area. For

example, if we set the cutting pore size as 13.8  $\mu\text{m}$ , cells with diameter larger than 13.8  $\mu\text{m}$  can be captured in the filter, which is indicated in the Figure 5.7. By calculating the ratio of red hashed area to the whole red area, we can get the yield of cancer cells which is 90.2%. Using same method, retention of leukocytes can be calculated by calculating blue area. Expected enrichment of size based separation with 13.8  $\mu\text{m}$  pore size can be derived by dividing retention of leukocytes from yield of cancer cells. By comparison with a model of cells as immutable spheres, we were able to calculate the expected enrichment that would be expected given the yield that we observed in our experiments (Table 5.7). As illustrated in Figure 5.8, we observed that the degree of enrichment, obtained by using ratchet mechanism, was consistently greater than would be expected due to size based sorting alone. Under the conditions examined, deformability contributes to a  $\sim 10$  to 100 fold increase in cell sorting sensitivity. Other size based sorting methods using deterministic lateral displacement (DLD), Dean Flow and dielectrophoresis (DEP) also show deficiency in enrichment ( $<100$ )<sup>40,41,43,54</sup>. These groups all use MCF-7 (average diameter 18-20 $\mu\text{m}$ <sup>41,43</sup>) doped samples in device characterization and obtained significant contamination of leukocytes, which resulted in limited enrichment of CTCs.

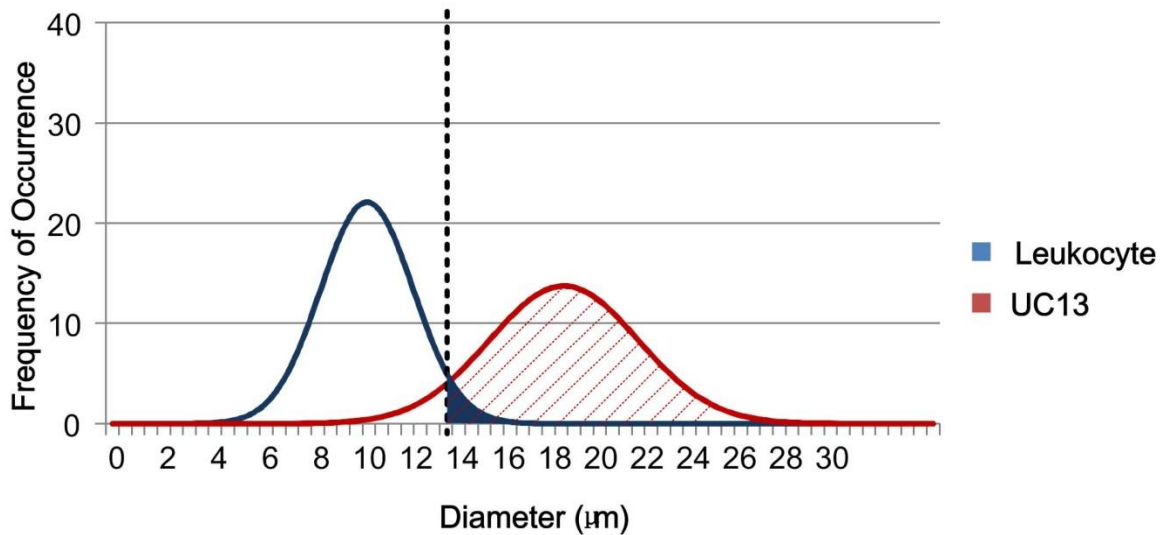


**Figure 5.7 Distributions of UC13 and leukocyte, and the method to calculate enrichment of size based separation with a pore size.**

**Table 5.7 Comparison of expected enrichment of size based separation and enrichment of separation using ratchet device when reaching the same yield.**

<b>Yield using ratchet device</b>	<b>Enrichment using ratchet device</b>	<b>Pore size for size-based method to reach the same yield</b>	<b>Retention of leukocytes</b>	<b>Enrichment using size-based methods</b>
<b>90.2%</b>	<b>5380</b>	13.8 $\mu\text{m}$	1.578%	<b>57</b>
<b>81.4%</b>	<b>8010</b>	15.0 $\mu\text{m}$	0.244%	<b>334</b>
<b>80.0%</b>	<b>10867</b>	15.2 $\mu\text{m}$	0.184%	<b>434</b>
<b>76.6%</b>	<b>13760</b>	15.5 $\mu\text{m}$	0.098%	<b>784</b>

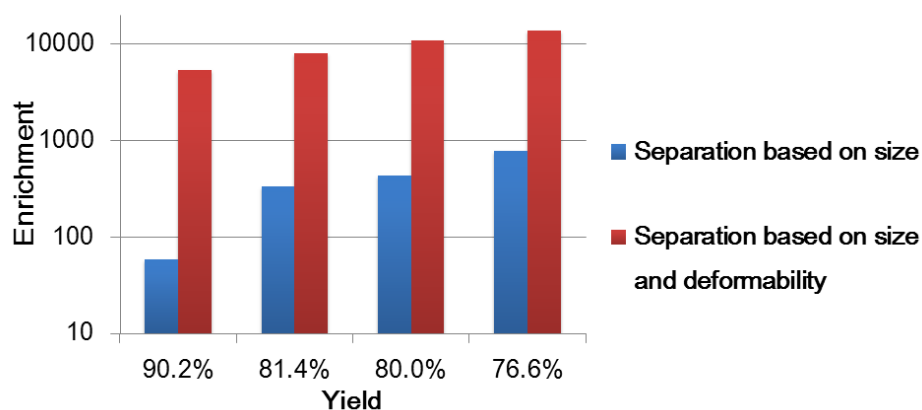


**Figure 5.8 Comparison of expected enrichment of size based separation and enrichment of separation using ratchet device when reaching the same yield.**

## 5.7 Discussion

We characterized the ability of this mechanism to separate rare cancer cells doped into leukocytes. Using different oscillation flow rates, the specificity (enrichment) and sensitivity (yield) of this mechanism can be adjusted. Specifically, at 90% yield, an enrichment  $>5,000$  can be achieved; while at the enrichment of 13,760, yield is  $>76\%$ . These values rival some of the best-reported results in this field. The ability to tradeoff sensitivity and specificity is a significant advantage that allows this mechanism to be adapted to the requirements of each application listed in the Section 1.3. Using the device with 32 rows by 2048 funnels in continuous processing mode, sample can be processed with a high throughput of 1 ml whole blood per hour ( $\sim 5 \times 10^6$  leukocytes per hour). Compared with

our previous version, which had  $32 \times 128$  funnels and operated in batch processing mode, throughput is increased by ~500 times.

Our microfluidic ratchet mechanism based cell separation system using a combination of size and deformability can achieve a ~10 to 100 fold increase in cell sorting sensitivity compared with size-only separation. As the circulating tumor cells share many physical and biological properties with cultured cancer cells including deformability, our size and deformability based method can make CTCs more distinguishable among background cells so as to achieve highly enriched CTC sample.

For the concentration limit of the device, our device shows capability in running blood with leukocytes' concentration ranging from  $4 \times 10^6$  to  $10 \times 10^6$  per ml. For the throughput of 1 ml/hour, our theoretical calculation of limit concentration is  $11.1 \times 10^6$  leukocytes per ml which is higher than normal human blood concentration.

In conclusion, our microfluidic device is capable of separating cancer cells from blood cells with high selectivity and high throughput, while maintaining the viability of the cell sample. Our experiments performed using cultured cancer cells optimized the system performance and demonstrated how deformability-based separation contributes to improved enrichment.

## Chapter 6: CTC Detection in Patient Samples

The workflow for processing patient blood samples is shown in Figure 6.1. The samples are always processed in microfluidic ratchet device within 24 hours after collected in EDTA tubes. After processing, samples collected in outlet were stained with immunofluorescent antibodies for overnight using standard staining procedures. After washing the sample the next day, samples were loaded into 384-well microplate (Corning®) for analysis under confocal microscope. We used the microfluidic ratchet device to enumerate CTCs from 58 samples with 52 patients with metastatic castrate resistant prostate cancer (mCRPC), in parallel with CellSearch, and 6 healthy control samples. The CTC capture rate is significantly higher for our device, which detected  $\geq 5$  CTCs in 67.3% of patients with an average count of 256, while the CellSearch system detected  $\geq 5$  CTCs in 40.4% of patients with an average count of 74.

Section 6.1 describes in detail the procedure involved in each step in the workflow. Section 6.1 describes the spectrum analysis technique used to detect CTCs. Finally Section 6.3 discusses the results on CTC detection from patients with castrate resistant prostate cancer using our microfluidic device and using the CellSearch system.

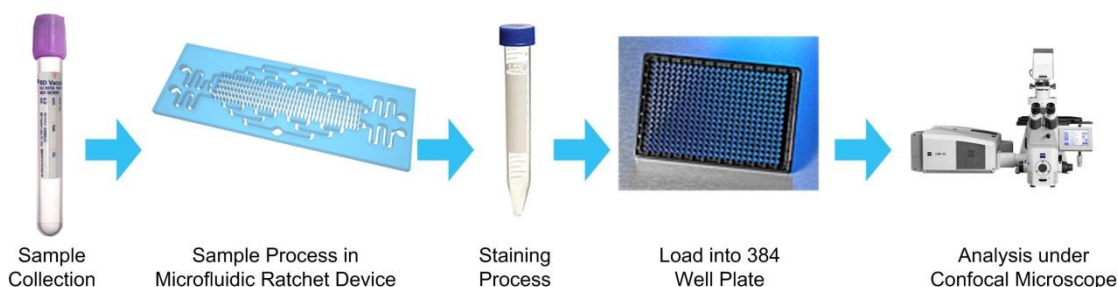


**Figure 6.1 Work flow of CTC separation using patient samples.**

### 6.1 Sample Preparation and Post-separation Analysis for Patient Samples

#### 6.1.1 Patient Sample Preparation

Patients with mCRPC were recruited by the BC Cancer Agency with informed consent. Blood samples of 5 ml were drawn from 52 patients seen at the clinics, as well as 6 healthy volunteers, and

processed using the ratchet device. The patient ages ranged from 49-92 years. All patients had failed initial therapy, mostly abiraterone or enzalutamide, and were either under ongoing treatment or at the end of treatment with a secondary therapy. The samples and healthy controls were blinded to prevent any bias during processing or counting. A 2 ml volume from of each blood sample was processed for CTC enumeration, while the rest was used for other tests.

### **6.1.2 Immunofluorescent Staining**

After processing the samples, cells in the CTC outlet were collected in a 15ml falcon tube and washed using PBS at 400xg for 5 minutes. Cells were then fixed with 3.5% PFS for 15 minutes and washed with PBS. A 0.5% concentration Tween 20 was added for 10 minutes to permeate the cells. After washing using PBS, the cells were blocked in 3% BSA for one hour at room temperature. Then, cells were incubated with antibody and conjugated at 4°C for overnight. Identification of CTCs based on a 4-color immunocytochemistry staining using Alexa 488-conjugated with anti-CK, Alexa 598-conjugated with anti-EpCAM, APC-conjugated with anti-CD45 (a marker for leukocytes), and DAPI DNA stain for the nucleus. In the following day, cells were washed with PBS for three times, stained with DAPI and then transferred to 384-well microplate (Corning®) for scanning. Prior to the patient study, these antibodies have been tested with cultured cancer cell lines (VCap) as positive control and healthy leukocytes as negative control.

### **6.1.3 Image Scanning and Analysis using Confocal Microscope**

A Zeiss® LSM 780 system was employed for image scanning and analysis. A whole well image was taken with an automated stage under a 40× oil objective (15 × 15 frames). PMT channel (DAPI), spectral channels (CK/EpCAM/CD45) and T-PMT channel (bright field) were taken in each frame. Spectral channels were binned into 32 colors for showing spectral peaks. Each antibody is conjugated with a different fluorophore, and therefore, each has a distinct absorption and emission wavelength. CK positive cells were selected and checked under spectral graphs. A cell with peak at 529 nm (CK-Alexa 488) emission wavelength and without peak at 660 nm (CD45-APC) would be considered CTC candidates (Figure 6.2). With or without peak at 617 nm (EpCAM- Alexa 598) would decide whether

the cell is EpCAM positive or negative. A cell with peak at 660nm (CD45-APC) would be depleted as leukocyte.

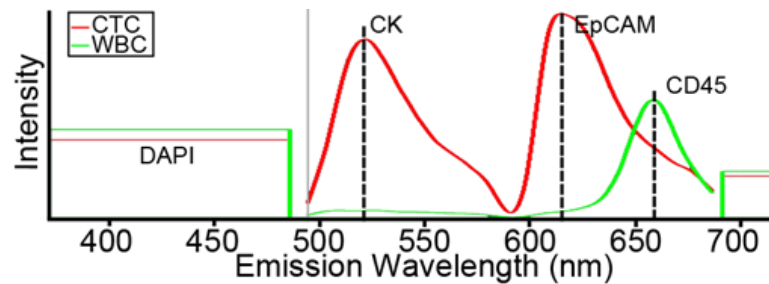


**Figure 6.2** Spectrum analysis for CTC identification. CTCs are identified with DAPI+, CK or EpCAM+, CD45-, while leukocytes are identified DAPI+, CK-, EpCAM- and CD45+.

## 6.2 Results from CRPC Patients

Comparison of captured CTC numbers between Microfluidic ratchet device and the CellSearch system is shown in Figure 6.3. In nearly all the samples, our microfluidic device detected more CTCs than CellSearch.

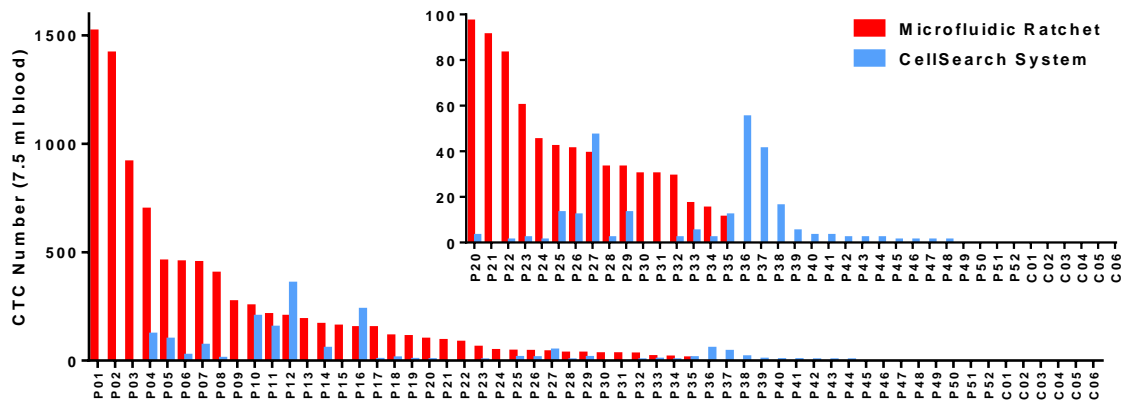


**Figure 6.3** Comparison of captured CTC numbers between Microfluidic ratchet device and CellSearch. P01 to P52 are patient samples; and C01 to C06 are healthy control samples.

Compared with CellSearch system, our microfluidic ratchet device found CTCs ( $\geq 5$ ) in 35/52 patients with an average count of 256, while CellSearch found CTCs ( $\geq 5$ ) in 21/52 with an average count of 74 (Table 6.1). In the 31 patients where CTCs were not found less than 5 by CellSearch, 18 were found with more than 5 CTCs by the microfluidic ratchet. In fact, 12 of these patients had CTC

counts from 60 to 1518.

**Table 6.1 Data comparison between Microfluidic ratchet device and CellSearch.**

	Microfluidic device	CellSearch
<b>% of CRPC patients with <math>\geq 5</math> CTCs in 7.5 ml of blood</b>	67.3%	40.4%
<b>Average number of CTCs for all CRPC samples</b>	172	30
<b>Average number of CTCs for samples with <math>\geq 5</math> CTCs</b>	256	74

40 of these 52 patients have clinical data showing whether the cancer is in progression or not compared with 12 weeks before. 18 out of these 40 patients have progression while the other 22 patients show stability or respond to treatments. Figure 6.4 shows comparison of captured CTC numbers between patients showing no progression and progression.

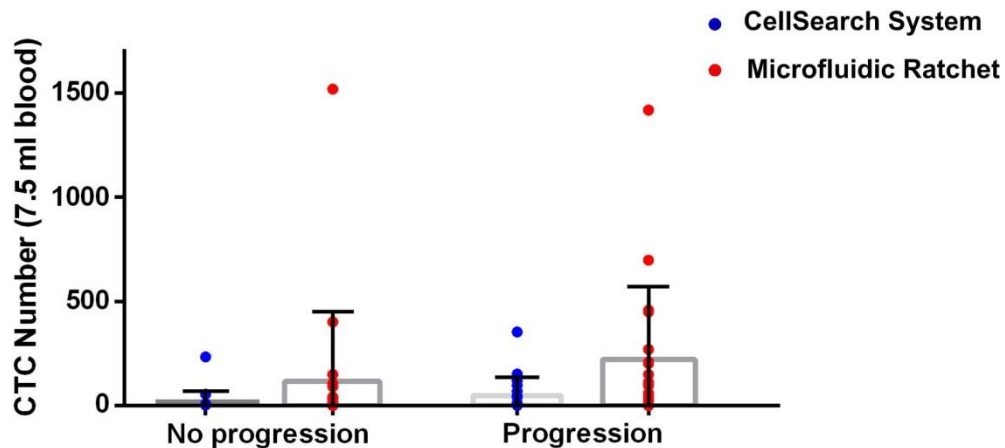


**Figure 6.4 Comparison of captured CTC numbers between patients showing no progression and progression in cancer using CellSearch system and Microfluidic ratchet device.**

CellSearch system detected a median number of 7.5 CTCs from patients showing progression and 2 CTCs from patients having no progression in cancer. However, our system found a median number of 104.5 CTCs from patients showing progression and 14 CTCs from patients having no progression in cancer. The results indicate that the CTC populations we captured are more related to cancer progression than the ones having high EpCAM expression.

CTCs found in these samples are all DAPI+, CK+, EpCAM+ and CD45- while leukocytes are

DAPI+, CD45+ (Figure 6.5). We also found some leukocytes with CK+ or EpCAM+. CTCs (average diameter: 9.97  $\mu\text{m}$ , deviation: 1.95  $\mu\text{m}$ ) are generally bigger than leukocytes (average diameter: 9.42  $\mu\text{m}$ , deviation: 0.86  $\mu\text{m}$ ) in the CTC outlet and have higher variation in size and shape. Nucleus shape and DAPI staining brightness also vary a lot.

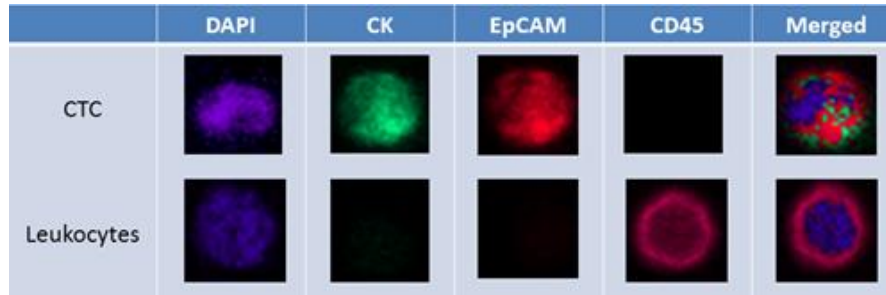


Figure 6.5 Example images of CTC and leukocyte.

## 6.3 Discussion

### 6.3.1 Confocal based Spectrum Analysis

In CellSearch assay, the CellTrack Analyzer generates the enriched cell images with 3 different channels (CK-PE/DAPI/CD45-APC) with one composite channel. A certified technician reviewed the images, and selects the positive tumor cells as CK+/DAPI+/CD45-. During this process, the technician might exclude some positive tumor cells with very bright CK channels, which might bleed over to CD45 channel, displaying CD45+ images. So many false negative cells will be excluded from CTC counting. In addition, some other groups also use CK conjugated with Alexa488, in which case the DAPI fluorescence signal could contribute to a false positive CTC identification by amplifying the CK signal. However our system involves a specialized confocal microscope with a sensor that captures up to 32 individual portions of the visible light spectrum. By using the recorded spectral response, the known spectra of various fluorophores can be identified even when their emission curves overlap.

### 6.3.2 EpCAM Expression

Although all CTCs that we found are EpCAM positive, expression level of EpCAM varies from different patients and cells. It has been previously recognized by other groups that CTCs within a

single patient can exhibit heterogeneous expression of EpCAM and microfluidic strategies have been employed to perform more sensitive immunoaffinity capture<sup>100</sup>. Low EpCAM expression is expected to accompany EMT, where tumor cells undergo a phenotypic switch that is accompanied by a loss of epithelial biomarkers, such as EpCAM, and a gain of mesenchymal markers. Because of the high sensitivity of the confocal microscope, low expression of EpCAM can also be detected. However in EpCAM based separation, there is a threshold level below which cells cannot be captured. These low EpCAM expression CTCs are thought to be more aggressive than high expression ones because of epithelial to mesenchymal transition.

In the 11 patients where CTCs were not found by CellSearch, we detected 207 CTCs in average and 5 of them had CTC counts from 90 to 1518. This discordance between CellSearch and our system may be attributed to the fact that CTCs that are enriched by microfluidic ratchet may express EpCAM below the threshold for efficient immunocapture.

## **Chapter 7: Conclusion**

### **7.1 Summary of Results**

We present a deformability based cell separation device capable of separating live circulating tumor cells from whole blood. This device is capable of log-4 depletion of leukocytes and 90% capture efficiency when tested using cultured cancer cells doped into whole blood. By using a continuous processing mode, our system is able to process 1 ml whole blood per hour which shows great improvement on previous version with batch processing mode. Cancer cells collected in our system still maintained high viability and proliferation capability. System characterization demonstrates significantly greater selectivity than separation based solely on size. This device successfully isolated circulating tumor cells from cancer patients with castrate-resistant prostate cancer and demonstrated significantly better performance than the CellSearch system. The results suggest that deformability based separation may select for distinct populations of CTCs than antigenic selection and our system is more suitable in analyzing patients with low EpCAM expression.

### **7.2 Limitations**

Our system has a throughput of 1 ml whole blood per hour, which is sufficiently fast for CTC enumeration. In the future, more CTC enriched samples are needed for post-separation analysis such as CTC culture, xenograft explants, and genome sequencing. We need to increase throughput so that >20 ml blood can be processed in a few hours. Parallelize 4 or 8 devices can solve problem, however there will be many tubes, tubing, and pressure control units. An integrated component which can combine single devices together but not adding peripheral components is required for processing large amount of patient samples in the future.

### **7.3 Future Works**

Our future work includes designing an integrated system that can operate multiple microfluidic devices together in parallel so that larger samples could be processed more quickly. This design

should integrate all tubes, tubing, and pressure control units inside the design to reduce set up time. Also the design should be easy to operate. Additionally, our work will focus on post-analysis of CTCs, including immunofluorescence, genomic sequencing, growing CTCs in culture, and xenograft explants.

## References

1. Ashworth, T. R. A case of cancer in which cells similar to those in the tumours were seen in the blood after death. *Med J Aust.* **14**, 146–149 (1869).
2. Norton, L. & Massagué, J. Is cancer a disease of self-seeding? *Nat. Med.* **12**, 875–878 (2006).
3. Mego, M., Mani, S. A. & Cristofanilli, M. Molecular mechanisms of metastasis in breast cancer—clinical applications. *Nat. Rev. Clin. Oncol.* **7**, 693–701 (2010).
4. Allard, W. J. *et al.* Tumor Cells Circulate in the Peripheral Blood of All Major Carcinomas but not in Healthy Subjects or Patients With Nonmalignant Diseases. *Clin. Cancer Res.* **10**, 6897–6904 (2004).
5. Miller, M. C., Doyle, G. V. & Terstappen, L. W. M. M. Significance of Circulating Tumor Cells Detected by the CellSearch System in Patients with Metastatic Breast Colorectal and Prostate Cancer. *J. Oncol.* **2010**, 617421 (2010).
6. Polyak, K. & Weinberg, R. A. Transitions between epithelial and mesenchymal states: acquisition of malignant and stem cell traits. *Nat. Rev. Cancer* **9**, 265–273 (2009).
7. Gossett, D. R. *et al.* Label-free cell separation and sorting in microfluidic systems. *Anal. Bioanal. Chem.* **397**, 3249–3267 (2010).
8. Schleip, K. Zur Diagnose von Knochenmarks- tumoren aus dem Blutbefunde. *Ztschr Klin Med* 261 (1906).
9. Ward, G. R. The Blood in Cancer with Bone Metastases. 676–677 (1913).
10. Marcus, H. Krebszellen im strömenden Blut? . *Ztschr Krebsforsch* 217 (1917).
11. Pool, E. H. & Dunlop, G. R. Cancer Cells in the Blood Stream. *Am. J. Cancer* **21**, 99–102 (1934).
12. Papanicolaou, G. & Traut, H. Diagnosis of uterine cancer by the vaginal smear. *J. Am. Med. Assoc.* **123**, 178–178 (1943).
13. Cole WH, P. D. Carcinoma of the colon with special reference to prevention of recurrence. *J. Am. Med. Assoc.* **155**, 1549–1553 (1954).
14. Engell, H. C. Cancer cells in the circulating blood; a clinical study on the occurrence of cancer cells in the peripheral blood and in venous blood draining the tumour area at operation. *Ugeskr. Laeger* **117**, 822–823 (1955).
15. Eriksson, O. Method for cytological detection of cancer cells in blood. *Cancer* **15**, 171–175 (1962).
16. Seal, S. H. Silicone flotation: A simple quantitative method for the isolation of free-floating cancer cells from the blood. *Cancer* **12**, 590–595 (1959).
17. Alexander, R. F. & Spriggs, A. I. The Differential Diagnosis of Tumour Cells in Circulating

- Blood. *J. Clin. Pathol.* **13**, 414–424 (1960).
18. Scheinin, T. M. & Koivuniemi, A. P. Large benign cells in circulating blood and their significance in the identification of cancer cells. *Cancer* **15**, 972–977 (1962).
  19. Roberts, S., Watne, A., McGrath, R., McGrew, E. & Cole, W. H. Technique and Results of Isolation of Cancer Cells From the Circulating Blood. *Obstet. Gynecol. Surv.* **13**, 745–747 (1958).
  20. Malmgren, R. A. in *Mech. Invasion Cancer* (ed. Denoix, P.) 108–117 (Springer Berlin Heidelberg, 1967). at [http://gw2jh3xr2c.scholar.serialssolutions.com/?sid=google&aunit=RA&aualast=Malmgren&atitle=Studies+of+circulating+cancer+cells+in+cancer+patients&id=doi:10.1007/978-3-642-87458-1\\_12](http://gw2jh3xr2c.scholar.serialssolutions.com/?sid=google&aunit=RA&aualast=Malmgren&atitle=Studies+of+circulating+cancer+cells+in+cancer+patients&id=doi:10.1007/978-3-642-87458-1_12)>
  21. Hsieh, H. B. *et al.* High speed detection of circulating tumor cells. *Biosens. Bioelectron.* **21**, 1893–1899 (2006).
  22. Marrinucci, D. *et al.* Case study of the morphologic variation of circulating tumor cells. *Hum. Pathol.* **38**, 514–519 (2007).
  23. Park, S. *et al.* Morphological Differences between Circulating Tumor Cells from Prostate Cancer Patients and Cultured Prostate Cancer Cells. *PLoS ONE* **9**, e85264 (2014).
  24. Hyun, K.-A., Kwon, K., Han, H., Kim, S.-I. & Jung, H.-I. Microfluidic flow fractionation device for label-free isolation of circulating tumor cells (CTCs) from breast cancer patients. *Biosens. Bioelectron.* **40**, 206–212 (2013).
  25. Marrinucci, D. *et al.* Circulating Tumor Cells From Well-Differentiated Lung Adenocarcinoma Retain Cytomorphologic Features of Primary Tumor Type. *Arch. Pathol. Lab. Med. Online* (2009). at <http://www.archivesofpathology.org/doi/abs/10.1043/1543-2165-133.9.1468>>
  26. Meng, S. *et al.* Circulating Tumor Cells in Patients with Breast Cancer Dormancy. *Clin. Cancer Res.* **10**, 8152–8162 (2004).
  27. Marrinucci, D. *et al.* Cytomorphology of Circulating Colorectal Tumor Cells: A Small Case Series. *J. Oncol.* **2010**, 1–7 (2010).
  28. Park, S. *et al.* Morphological Differences Between Circulating Tumour Cells from Prostate Cancer Patients and Cultured Prostate Cancer Cells. *Submitted* (2013).
  29. Gascoyne, P. R. C., Shim, S., Noshari, J., Becker, F. F. & Stemke-Hale, K. Correlations between the dielectric properties and exterior morphology of cells revealed by dielectrophoretic field-flow fractionation. *ELECTROPHORESIS* **34**, 1042–1050 (2013).
  30. Guilak, F., Tedrow, J. R. & Burgkart, R. Viscoelastic Properties of the Cell Nucleus. *Biochem. Biophys. Res. Commun.* **269**, 781–786 (2000).
  31. Guo, Q., Park, S. & Ma, H. Microfluidic micropipette aspiration for measuring the deformability of single cells. *Lab. Chip* **12**, 2687 (2012).
  32. Rosenbluth, M. J., Lam, W. A. & Fletcher, D. A. Force Microscopy of Nonadherent Cells: A

- Comparison of Leukemia Cell Deformability. *Biophys. J.* **90**, 2994–3003 (2006).
33. Cross, S. E., Jin, Y.-S., Rao, J. & Gimzewski, J. K. Nanomechanical analysis of cells from cancer patients. *Nat. Nanotechnol.* **2**, 780–783 (2007).
  34. Weiss, L. & Schmid-Schönbein, G. W. Biomechanical interactions of cancer cells with the microvasculature during metastasis. *Cell Biophys.* **14**, 187–215 (1989).
  35. Beech, J. P., Holm, S. H., Adolfsson, K. & Tegenfeldt, J. O. Sorting cells by size, shape and deformability. *Lab. Chip* **12**, 1048 (2012).
  36. Loutharback, K. *et al.* Deterministic separation of cancer cells from blood at 10 mL/min. *AIP Adv.* **2**, 042107 (2012).
  37. Carlo, D. D. Inertial microfluidics. *Lab. Chip* **9**, 3038–3046 (2009).
  38. Inglis, D. W. Efficient microfluidic particle separation arrays. *Appl. Phys. Lett.* **94**, 013510 (2009).
  39. Huang, L. R., Cox, E. C., Austin, R. H. & Sturm, J. C. Continuous particle separation through deterministic lateral displacement. *Science* **304**, 987–990 (2004).
  40. Liu, Z. *et al.* Rapid isolation of cancer cells using microfluidic deterministic lateral displacement structure. *Biomicrofluidics* **7**, 011801 (2013).
  41. Sun, J. *et al.* Double spiral microchannel for label-free tumor cell separation and enrichment. *Lab. Chip* **12**, 3952 (2012).
  42. Hou, H. W. *et al.* Isolation and retrieval of circulating tumor cells using centrifugal forces. *Sci. Rep.* **3**, 1259 (2013).
  43. Hur, S. C., Mach, A. J. & Di Carlo, D. High-throughput size-based rare cell enrichment using microscale vortices. *Biomicrofluidics* **5**, 022206 (2011).
  44. Moon, H.-S. *et al.* Continual collection and re-separation of circulating tumor cells from blood using multi-stage multi-orifice flow fractionation. *Biomicrofluidics* **7**, 014105 (2013).
  45. Bhagat, A. A. S., Hou, H. W., Li, L. D., Lim, C. T. & Han, J. Pinched flow coupled shear-modulated inertial microfluidics for high-throughput rare blood cell separation. *Lab. Chip* **11**, 1870 (2011).
  46. Carlo, D. D., Irimia, D., Tompkins, R. G. & Toner, M. Continuous inertial focusing, ordering, and separation of particles in microchannels. *Proc. Natl. Acad. Sci.* **104**, 18892–18897 (2007).
  47. Bhagat, A. A. S., Kuntaegowdanahalli, S. S. & Papautsky, I. Continuous particle separation in spiral microchannels using Dean flows and differential migration. *Lab. Chip* **8**, 1906–1914 (2008).
  48. Wang, X.-B. *et al.* Changes in Friend murine erythroleukaemia cell membranes during induced differentiation determined by electrorotation. *Biochim. Biophys. Acta BBA - Biomembr.* **1193**, 330–344 (1994).
  49. Yang, J. *et al.* Dielectric Properties of Human Leukocyte Subpopulations Determined by Electrorotation as a Cell Separation Criterion. *Biophys. J.* **76**, 3307–3314 (1999).

50. Doh, I. & Cho, Y.-H. A continuous cell separation chip using hydrodynamic dielectrophoresis (DEP) process. *Sens. Actuators Phys.* **121**, 59–65 (2005).
51. Yang, J., Huang, Y., Wang, X.-B., Becker, F. F. & Gascoyne, P. R. C. Cell Separation on Microfabricated Electrodes Using Dielectrophoretic/Gravitational Field-Flow Fractionation. *Anal. Chem.* **71**, 911–918 (1999).
52. Alazzam, A., Stiharu, I., Bhat, R. & Meguerditchian, A.-N. Interdigitated comb-like electrodes for continuous separation of malignant cells from blood using dielectrophoresis. *ELECTROPHORESIS* **32**, 1327–1336 (2011).
53. Gascoyne, P. R. C., Noshari, J., Anderson, T. J. & Becker, F. F. Isolation of rare cells from cell mixtures by dielectrophoresis. *ELECTROPHORESIS* **30**, 1388–1398 (2009).
54. Moon, H.-S. *et al.* Continuous separation of breast cancer cells from blood samples using multi-orifice flow fractionation (MOFF) and dielectrophoresis (DEP). *Lab. Chip* **11**, 1118 (2011).
55. Shim, S. *et al.* Antibody-independent isolation of circulating tumor cells by continuous-flow dielectrophoresis. *Biomicrofluidics* **7**, 011807–011807–12 (2013).
56. Beattie, W., Qin, X., Wang, L. & Ma, H. Clog-free cell filtration using resettable cell traps. *Lab. Chip* **14**, 2657 (2014).
57. Gerhardt, T., Woo, S. & Ma, H. Chromatographic behaviour of single cells in a microchannel with dynamic geometry. *Lab. Chip* **11**, 2731 (2011).
58. Ji, H. M. *et al.* Silicon-based microfilters for whole blood cell separation. *Biomed. Microdevices* **10**, 251–257 (2008).
59. McFaul, S. M., Lin, B. K. & Ma, H. Cell separation based on size and deformability using microfluidic funnel ratchets. *Lab. Chip* **12**, 2369 (2012).
60. Tan, S. J. *et al.* Versatile label free biochip for the detection of circulating tumor cells from peripheral blood in cancer patients. *Biosens. Bioelectron.* **26**, 1701–1705 (2010).
61. Lu, B., Xu, T., Zheng, S., Goldkorn, A. & Tai, Y.-C. Parylene membrane slot filter for the capture, analysis and culture of viable circulating tumor cells. in *2010 IEEE 23rd Int. Conf. Micro Electro Mech. Syst. MEMS* 935–938 (2010). doi:10.1109/MEMSYS.2010.5442361
62. Lin, H. K. *et al.* Portable Filter-Based Microdevice for Detection and Characterization of Circulating Tumor Cells. *Clin. Cancer Res.* **16**, 5011–5018 (2010).
63. Zheng, S. *et al.* Membrane microfilter device for selective capture, electrolysis and genomic analysis of human circulating tumor cells. *J. Chromatogr. A* **1162**, 154–161 (2007).
64. Zheng, S. *et al.* 3D microfilter device for viable circulating tumor cell (CTC) enrichment from blood. *Biomed. Microdevices* **13**, 203–213 (2011).
65. Kuo, J. S. *et al.* Deformability considerations in filtration of biological cells. *Lab. Chip* **10**, 837 (2010).
66. Seal, S. H. A sieve for the isolation of cancer cells and other large cells from the blood. *Cancer*

- 17**, 637–642 (1964).
67. Vona, G. *et al.* Isolation by Size of Epithelial Tumor Cells: A New Method for the Immunomorphological and Molecular Characterization of Circulating Tumor Cells. *Am. J. Pathol.* **156**, 57–63 (2000).
  68. Lin, B. K., McFaul, S. M., Jin, C., Black, P. C. & Ma, H. Highly selective biomechanical separation of cancer cells from leukocytes using microfluidic ratchets and hydrodynamic concentrator. *Biomicrofluidics* **7**, 034114–034114–11 (2013).
  69. Ma, Y.-C., Wang, L. & Yu, F.-L. Recent Advances and Prospects in the Isolation by Size of Epithelial Tumor Cells (ISET) Methodology. *Technol. Cancer Res. Treat.* **12**, 295–309 (2013).
  70. Desitter, I. *et al.* A new device for rapid isolation by size and characterization of rare circulating tumor cells. *Anticancer Res.* **31**, 427–441 (2011).
  71. Lim, E., Tay, A. & Nicholson, A. G. Antibody independent microfluidic cell capture of circulating tumor cells for the diagnosis of cancer. *J. Thorac. Oncol. Off. Publ. Int. Assoc. Study Lung Cancer* **7**, e42–43 (2012).
  72. De Giorgi, V. *et al.* Application of a filtration- and isolation-by-size technique for the detection of circulating tumor cells in cutaneous melanoma. *J. Invest. Dermatol.* **130**, 2440–2447 (2010).
  73. Pinzani, P. *et al.* DETECTION OF CIRCULATING TUMOR CELLS IN PATIENTS WITH ADRENOCORTICAL CARCINOMA: A MONOCENTRIC PRELIMINARY STUDY. *J. Clin. Endocrinol. Metab.* (2013). doi:10.1210/jc.2013-1396
  74. Hofman, V. *et al.* Preoperative circulating tumor cell detection using the isolation by size of epithelial tumor cell method for patients with lung cancer is a new prognostic biomarker. *Clin. Cancer Res. Off. J. Am. Assoc. Cancer Res.* **17**, 827–835 (2011).
  75. Armstrong, A. J. *et al.* Circulating Tumor Cells from Patients with Advanced Prostate and Breast Cancer Display Both Epithelial and Mesenchymal Markers. *Mol. Cancer Res.* **9**, 997–1007 (2011).
  76. Gravdal, K., Halvorsen, O. J., Haukaas, S. A. & Akhlen, L. A. A Switch from E-Cadherin to N-Cadherin Expression Indicates Epithelial to Mesenchymal Transition and Is of Strong and Independent Importance for the Progress of Prostate Cancer. *Clin. Cancer Res.* **13**, 7003–7011 (2007).
  77. Zhu, L. *et al.* Prominin 1 marks intestinal stem cells that are susceptible to neoplastic transformation. *Nature* **457**, 603–607 (2009).
  78. Nieva, J. *et al.* High definition imaging of circulating tumor cells and associated cellular events in non-small cell lung cancer patients; a longitudinal analysis. *Phys. Biol.* **9**, 016004 (2012).
  79. Marrinucci, D. *et al.* Fluid biopsy in patients with metastatic prostate, pancreatic and breast cancers. *Phys. Biol.* **9**, 016003 (2012).
  80. Mayer, J. A. *et al.* FISH-based determination of HER2 status in circulating tumor cells isolated with the microfluidic CEE™ platform. *Cancer Genet.* **204**, 589–595 (2011).

81. Leversha, M. A. *et al.* Fluorescence in situ hybridization analysis of circulating tumor cells in metastatic prostate cancer. *Clin. Cancer Res. Off. J. Am. Assoc. Cancer Res.* **15**, 2091–2097 (2009).
82. Heitzer, E. *et al.* Complex Tumor Genomes Inferred from Single Circulating Tumor Cells by Array-CGH and Next-Generation Sequencing. *Cancer Res.* (2013). doi:10.1158/0008-5472.CAN-12-4140
83. Iakovlev, V. V., Goswami, R. S., Vecchiarelli, J., Arneson, N. C. R. & Done, S. J. Quantitative detection of circulating epithelial cells by Q-RT-PCR. *Breast Cancer Res. Treat.* **107**, 145–154 (2007).
84. Devriese, L. A. *et al.* Circulating tumor cell detection in advanced non-small cell lung cancer patients by multi-marker QPCR analysis. *Lung Cancer* **75**, 242–247 (2012).
85. Louha, M. *et al.* Liver resection and needle liver biopsy cause hematogenous dissemination of liver cells. *Hepatology* **29**, 879–882 (1999).
86. Yie, S.-M., Luo, B., Ye, N.-Y., Xie, K. & Ye, S.-R. Detection of Survivin-expressing circulating cancer cells in the peripheral blood of breast cancer patients by a RT-PCR ELISA. *Clin. Exp. Metastasis* **23**, 279–289 (2006).
87. Punnoose, E. A. *et al.* Evaluation of Circulating Tumor Cells and Circulating Tumor DNA in Non-Small Cell Lung Cancer: Association with Clinical Endpoints in a Phase II Clinical Trial of Pertuzumab and Erlotinib. *Clin. Cancer Res.* **18**, 2391–2401 (2012).
88. Carlo, D. D. A Mechanical Biomarker of Cell State in Medicine. *J. Lab. Autom.* **17**, 32–42 (2012).
89. Vadillo-Rodriguez, V., Beveridge, T. J. & Dutcher, J. R. Surface Viscoelasticity of Individual Gram-Negative Bacterial Cells Measured Using Atomic Force Microscopy. *J. Bacteriol.* **190**, 4225–4232 (2008).
90. Engelhardt, H., Gaub, H. & Sackmann, E. Viscoelastic properties of erythrocyte membranes in high-frequency electric fields. *Nature* **307**, 378–380 (1984).
91. Zimmermann, U. *et al.* Electromanipulation of mammalian cells: fundamentals and application. *IEEE Trans. Plasma Sci.* **28**, 72–82 (2000).
92. Ashkin, A., Dziedzic, J. M. & Yamane, T. Optical trapping and manipulation of single cells using infrared laser beams. *Nature* **330**, 769–771 (1987).
93. Kaneta, T., Makihara, J. & Imasaka, T. An ‘Optical Channel’: A Technique for the Evaluation of Biological Cell Elasticity. *Anal. Chem.* **73**, 5791–5795 (2001).
94. Guo, Q., McFaul, S. M. & Ma, H. Deterministic microfluidic ratchet based on the deformation of individual cells. *Phys. Rev. E* **83**, 051910 (2011).
95. Lin, B. K., McFaul, S. M., Jin, C., Black, P. C. & Ma, H. Highly selective biomechanical separation of cancer cells from leukocytes using microfluidic ratchets and hydrodynamic

- concentrator. *Biomicrofluidics* **7**, 034114 (2013).
96. Lim, C. T., Zhou, E. H. & Quek, S. T. Mechanical models for living cells—a review. *J. Biomech.* **39**, 195–216 (2006).
  97. Haines, W. B. Studies in the physical properties of soil. V. The hysteresis effect in capillary properties, and the modes of moisture distribution associated therewith. *J. Agric. Sci.* **20**, 97–116 (1930).
  98. Mohamed, H., Murray, M., Turner, J. N. & Caggana, M. Isolation of tumor cells using size and deformation. *J. Chromatogr. A* **1216**, 8289–8295 (2009).
  99. Lim, L. S. *et al.* Microsieve lab-chip device for rapid enumeration and fluorescence in situ hybridization of circulating tumor cells. *Lab. Chip* **12**, 4388 (2012).
  100. Ozkumur, E. *et al.* Inertial Focusing for Tumor Antigen–Dependent and –Independent Sorting of Rare Circulating Tumor Cells. *Sci. Transl. Med.* **5**, 179ra47–179ra47 (2013).